

This is the author-created version of the following work:

Bishop-Taylor, Robbi, Sagar, Stephen, Lymburner, Leo, and Beaman, Robin J. (2019) *Between the tides: modelling the elevation of Australia's exposed intertidal zone at continental scale*. Estuarine, Coastal and Shelf Science, . (In Press)

Access to this file is available from:

<https://researchonline.jcu.edu.au/57784/>

Copyright © 2019. This manuscript version is made available under the CC-BY-NC-ND 4.0 license <http://creativecommons.org/licenses/by-nc-nd/4.0/>

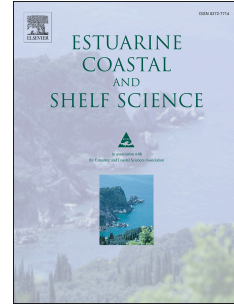
Please refer to the original source for the final version of this work:

<https://doi.org/10.1016/j.ecss.2019.03.006>

Accepted Manuscript

Between the tides: Modelling the elevation of Australia's exposed intertidal zone at continental scale

Robbi Bishop-Taylor, Stephen Sagar, Leo Lymburner, Robin J. Beaman



PII: S0272-7714(18)30878-3

DOI: <https://doi.org/10.1016/j.ecss.2019.03.006>

Reference: YECSS 6149

To appear in: *Estuarine, Coastal and Shelf Science*

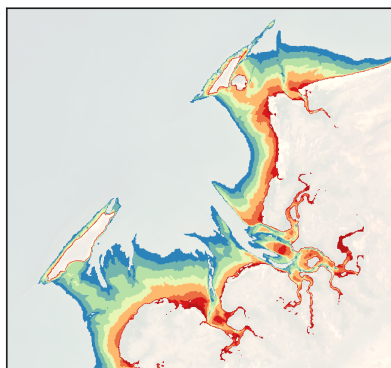
Received Date: 18 October 2018

Revised Date: 12 March 2019

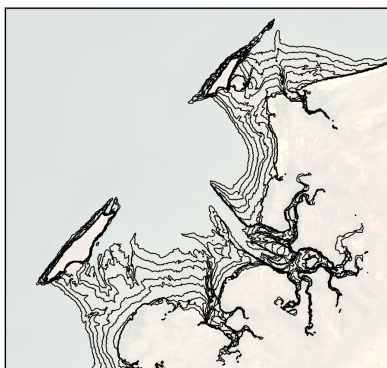
Accepted Date: 12 March 2019

Please cite this article as: Bishop-Taylor, R., Sagar, S., Lymburner, L., Beaman, R.J., Between the tides: Modelling the elevation of Australia's exposed intertidal zone at continental scale, *Estuarine, Coastal and Shelf Science* (2019), doi: <https://doi.org/10.1016/j.ecss.2019.03.006>.

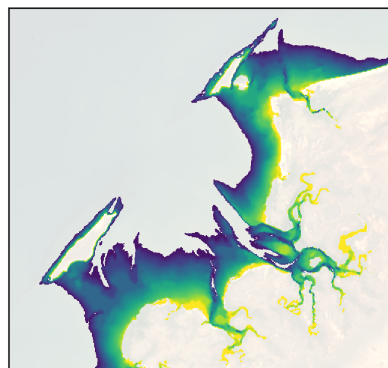
This is a PDF file of an unedited manuscript that has been accepted for publication. As a service to our customers we are providing this early version of the manuscript. The manuscript will undergo copyediting, typesetting, and review of the resulting proof before it is published in its final form. Please note that during the production process errors may be discovered which could affect the content, and all legal disclaimers that apply to the journal pertain.



10% intervals of the tidal range mapped from 30 years of Landsat satellite imagery



Waterline contours extracted and assigned median tidal heights for each 10% interval



Interpolated elevation relative to mean sea level
< 2.50 m 0.00 m > 1.50 m

ACCEPTED MANUSCRIPT

1 Between the tides: modelling the elevation of
2 Australia's exposed intertidal zone at continental
3 scale

4
5 Robbi Bishop-Taylor (Robbi.Bishop-Taylor@ga.gov.au)^a

6 Stephen Sagar (Stephen.Sagar@ga.gov.au)^a

7 Leo Lymburner (Leo.Lymburner@ga.gov.au)^a

8 Robin J. Beaman (robin.beaman@jcu.edu.au)^b

9

10 ^a Geoscience Australia

11 101 Jerrabomberra Ave, Symonston ACT 2609 Australia

12

13 ^b College of Science and Engineering, James Cook University,

14 Cairns QLD 4870 Australia

15

16 Corresponding author: Robbi Bishop-Taylor

17 Email address: Robbi.Bishop-Taylor@ga.gov.au

18 **Abstract**

19 The intertidal zone represents a critical transition between marine and terrestrial
20 ecosystems, supporting a complex mosaic of highly productive and biologically diverse
21 habitats. However, our understanding of these important coastal environments is limited by a
22 lack of spatially consistent topographic data, which can be extremely challenging and costly
23 to obtain at continental-scale. Satellite remote sensing represents an important resource for
24 monitoring extensive coastal zones. Previous approaches to modelling the elevation of the
25 intertidal zone using earth observation (EO) data have been restricted to small study regions
26 or have relied on manual image interpretation, thus limiting their ability to be applied
27 consistently over large geographic extents. In this study, we present an automated open-
28 source approach to generate satellite-derived elevation data for over 15,387 km² of intertidal
29 terrain across the entire Australian coastline. Our approach combines global tidal modelling
30 with a 30-year time series archive of spatially and spectrally calibrated Landsat satellite data
31 managed within the Digital Earth Australia (DEA) platform. The resulting National Intertidal
32 Digital Elevation Model (NIDEM) dataset provides an unprecedented three-dimensional
33 representation of Australia's vast exposed intertidal zone at 25 m spatial resolution. We
34 validate our model against LiDAR, RTK GPS and multibeam bathymetry datasets, finding
35 that modelled elevations are highly accurate across sandy beach (± 0.41 m RMSE) and tidal
36 flat environments (± 0.39 m RMSE). Model performance was least accurate (± 2.98 m
37 RMSE) within rocky shores and reefs and other complex coastal environments with extreme
38 and variable tidal regimes. We discuss key challenges associated with modelling intertidal
39 elevation including tidal model performance and biased observations from sun-synchronous
40 satellites, and suggest future directions to improve the accuracy and utility of continental-
41 scale intertidal elevation modelling. Our model can be applied to tidally-influenced coastal
42 environments globally, addressing a key gap between the availability of sub-tidal bathymetry
43 and terrestrial elevation data.

44 Highlights

- 45 ● The intertidal zone supports critical but increasingly threatened ecosystems
- 46 ● The topography of the intertidal zone remains poorly mapped globally
- 47 ● We present the first continental-scale digital elevation model (DEM) of the intertidal zone
- 48 ● Our approach combines global tidal modelling with 30 years of Landsat satellite data
- 49 ● The resulting DEM provides a critical link between terrestrial elevation and bathymetric
- 50 datasets

51 Keywords

52 Digital elevation model, Intertidal zone, Remote sensing, Continental-scale, Tidal modelling,
53 Australia, Landsat

54 Introduction

55 The intertidal zone - the area of coastline periodically exposed and inundated by tides -
56 represents a critical transition between marine and terrestrial ecosystems. Intertidal
57 environments support a complex mosaic of extremely productive and biodiverse habitats
58 ranging from extensive tidal mudflats, sandy beaches, fringing coral reefs and steep rocky
59 cliffs (Banks et al., 2005; Luijendijk et al., 2018). Due to the influence of tidal processes,
60 organisms inhabiting the intertidal zone are typically adapted to extremely dynamic
61 conditions and display strong zonation by elevation along the environmental gradient from
62 permanently to occasionally inundated terrain (Bearup and Blasius, 2017). Because of their
63 high ecological diversity and productivity, intertidal zones serve as key feeding grounds for
64 many endangered shorebird species that use them as critical 'stop-over' points while
65 undertaking cross-continental migrations (Murray et al., 2015; Xia et al., 2017). In addition to
66 their ecological value, intertidal zones also provide many economically significant ecosystem
67 services, including nutrient cycling and carbon storage (Chmura et al., 2003; Billerbeck et al.,
68 2006), storm surge protection (Temmerman et al., 2013), and natural resources for
69 recreational and commercial use (Barbier et al., 1997; Chen et al., 2016). Intertidal zones,
70 however, are also among the world's most vulnerable and threatened ecosystems, with land
71 reclamation, changes in river sediment balances and coastal erosion representing key
72 threatening processes responsible for a global reduction in intertidal extent of up to 16%
73 between 1984 and 2016 (Murray et al., 2018). Given their low relief, intertidal zones are also
74 likely to be disproportionately affected by global sea-level rise, which is expected to
75 accelerate throughout the 21st century (Galbraith et al., 2002; Kirwan and Megonigal, 2013;
76 Li and Gong, 2016).

77

78 Understanding, predicting and managing the impacts of these processes on intertidal
79 ecosystems requires detailed data on the distribution and structure of these habitats across
80 ecologically relevant spatial extents. However, the three-dimensional topography of the
81 intertidal zone remains poorly mapped globally (Eakins and Grothe, 2014; Tseng et al.,
82 2017). Due to the impermeability of water to radar transmission and a lack of repeated
83 observations over tidally-influenced terrain, global digital elevation models (DEMs) produced
84 using Synthetic Aperture Radar (e.g. TerraSAR-X/TanDEM-X WorldDEM and Shuttle Radar
85 Topography Mission DEM or SRTM) or stereo-pair optical imagery (e.g. Aster GDEM) are
86 typically restricted to the terrestrial domain (Eakins and Grothe, 2014; Tseng et al., 2017).
87 Similarly, intertidal zones are regularly omitted from bathymetric models produced using
88 acoustic techniques due to the difficulty of surveying safely from vessels in shallow coastal
89 waters (Hogrefe et al., 2008; Eakins and Grothe, 2014; Weatherall et al., 2015). When

90 combined with hazardous ground survey conditions caused by dynamic tidal processes, this
91 has resulted in a significant gap in the elevation data available across the land-sea interface
92 (Hogrefe et al., 2008; Eakins and Grothe, 2014). Airborne Light Detection and Ranging
93 (LiDAR) bathymetry surveys have shown promise as an approach to address this gap, being
94 capable of rapidly generating accurate, high-resolution bathymetry data at depths of up to 70
95 m in clear water (Su et al., 2008). However, the reliability of these systems can be strongly
96 influenced by turbidity and breaking white water that frequently affect shallow coastal zone
97 waters, and their high acquisition cost usually limits applications to local- or regional-scales
98 (Su et al., 2008; Gao, 2009; Klemas, 2011).

99
100 Temporal 'waterline' methods based on satellite remote sensing represent an alternative
101 approach to modelling the elevation of the intertidal zone (Mason et al., 1997; Chen and
102 Rau, 1998). The rise and fall of the ocean can be used to describe the three-dimensional
103 topography of the coastline by mapping the location of the waterline as a series of
104 topographic contours that cover a range of tidal stages (Zhao et al., 2008; Tseng et al.,
105 2017). Assuming that each waterline represents a constant elevation relative to mean sea
106 level (MSL), these contours can be tagged with tide heights and then interpolated to produce
107 a DEM covering the elevation range between the highest and lowest observed tide (Ryu et
108 al., 2008). Satellites such as the United States Geological Survey (USGS) Landsat mission
109 have continuously monitored coastal zones globally since 1972, providing the temporal
110 depth and resolution required to obtain dense observations across the full tidal range (Boak
111 and Turner, 2005; Gens, 2010). Accordingly, temporal stacks of satellite imagery have been
112 combined with tidal modelling to produce tidally-tagged time series of the coastline for DEM
113 generation (e.g. Mason et al., 1997; Chen and Rau, 1998; Ryu et al., 2008; Zhao et al.,
114 2008; Chen and Chang, 2009; Liu et al., 2013a, 2013b; Xu et al., 2016; Tseng et al., 2017).
115 However, due to challenge of extracting waterline contours from large numbers of remotely-
116 sensed images, previous approaches have extracted waterlines from a limited selection of
117 images using manual digitisation and visual interpretation (e.g. Chen and Rau, 1998; Zhao
118 et al., 2008; Liu et al., 2013b; Chen et al., 2016). Although these manually digitised contours
119 can produce highly accurate DEMs (e.g. less than 0.4 m RMSE compared to LiDAR; Liu et
120 al., 2013b), this manual process introduces subjectivity, is impractical to apply at a
121 continental-scale, and is restricted by availability of high quality observations covering the
122 entire tidal range.

123
124 There is a recognised need for more objective and robust approaches to waterline extraction
125 and intertidal DEM generation that can be applied consistently across space and time (Boak
126 and Turner, 2005). Such approaches are likely to require leveraging the full temporal record

127 of available global-extent earth observation (EO) data. While satellite data with long temporal
128 records such as the Landsat archive were formerly prohibitively expensive to apply at
129 continental-scale, the USGS free-data policy in 2008 has significantly lowered barriers to
130 obtaining EO data (Woodcock et al., 2008; Wulder et al., 2012). More recently, the creation
131 of archives of analysis-ready data or ARD (Dwyer et al., 2018) combined with high-
132 performance computing platforms have provided unprecedented access to petabytes of
133 geometrically and spectrally calibrated satellite imagery (Lewis et al., 2016). ARD archives
134 and analysis platforms such as Digital Earth Australia (Dhu et al., 2017), Google Earth
135 Engine (Gorelick et al., 2017) and the upcoming Copernicus Data and Information Access
136 Services provide satellite observations that can be analysed and compared consistently
137 across space and time. This has driven a new wave of scientific applications that leverage
138 multiple decades of data to analyse extremely large areas of the Earth's surface (e.g.
139 Mueller et al., 2016; Hermosilla et al., 2017; Bugnot et al., 2018; Egorov et al., 2018;
140 Luijendijk et al., 2018). These developments make it practical for the first time to implement
141 automated waterline extraction and intertidal elevation modelling at the continental-scale.

142

143 In this study, we present an open-source workflow for deriving elevation data for the
144 intertidal zone of Australia. We leverage the full 30-year archive of analysis-ready Landsat
145 data managed within the Digital Earth Australia (DEA) platform that provides spatially and
146 spectrally calibrated EO data, enabling time-series analysis on a per-pixel basis across the
147 entire Australian continent. We combine this archive with a newly developed multi-resolution
148 tidal modelling framework that accurately associates each satellite observation with
149 modelled tide heights. The resulting National Intertidal Digital Elevation Model (NIDEM;
150 Bishop-Taylor et al., 2018) is a continental-scale dataset providing the first 25 m resolution,
151 three-dimensional representation of Australia's exposed intertidal environments including
152 tidal flats, sandy beaches and shores, and rocky shores and reefs. We anticipate that
153 NIDEM will complement existing intertidal extent products and support a new suite of use
154 cases that require a more detailed understanding of the three-dimensional topography of the
155 intertidal zone, such as hydrodynamic modelling, coastal risk management and ecological
156 habitat mapping projects.

157 Methods

158 Relative intertidal extents

159 The foundation of NIDEM is the continental-scale Intertidal Extents Model (ITEM v1.0)
160 developed by Sagar et al., 2017, derived from a 30-year time series archive of Landsat
161 observations. The Landsat archive is managed within the Digital Earth Australia (DEA)
162 platform, combining high performance computing with the concept of spatiotemporally
163 consistent ARD (Dhu et al., 2017). These data are processed to surface reflectance utilising
164 a standardised atmospheric and geometric correction workflow to enable operational
165 analysis (Lewis et al., 2016). The ITEM process is based on sorting all observations in the
166 Landsat archive by tide height, binning observations into ten percent intervals of the
167 observed tidal range, then mapping the typical location of the waterline across a range of
168 tidal stages using Normalised Difference Water Index composite images (NDWI; McFeeters,
169 1996). NDWI is a remote sensing index designed to detect open water by taking advantage
170 of the high reflectance of visible green light and low reflectance of near-infrared radiation
171 (NIR) by water, and the high reflectance of NIR by dry soil and terrestrial vegetation:

$$NDWI = \frac{(Green - NIR)}{(Green + NIR)}$$

173
174 Although NDWI has been used extensively to monitor the intertidal zone (e.g. Murray et al.,
175 2012; Dhanjal-Adams et al., 2016; Fan et al., 2018; Luijendijk et al., 2018), NIR bands can
176 be affected by white water near the land-water boundary (Kelly and Gontz, 2018; Pardo-
177 Pascual et al., 2018). Other indices such as the Modified Normalised Difference Water Index
178 (MNDWI; Xu, 2006) have shown promise for monitoring the intertidal zone by utilising short-
179 wave infrared (SWIR) in place of NIR (e.g. Wang et al., 2018; Xu, 2018). However, SWIR-
180 based indices have been found to significantly misrepresent the location of the waterline
181 across exposed tidal flats where water remains during ebb tides (Ryu et al., 2002, 2008). To
182 ensure waterlines could be consistently extracted from imagery across tidal stages and
183 intertidal environments that included extensive tidal flats, NDWI was selected and applied to
184 all Landsat observations within each ten percent tidal interval. These individual NDWI layers
185 were then combined into composites for each tidal interval by taking the median NDWI value
186 per pixel, and classified to produce water vs. non-water layers that represented typical
187 waterlines locations from the lowest to the highest observed tides (Figure 2a).

188

189 In this study, we further develop the initial model (ITEM v1.0) described in Sagar et al.
190 (2017) by leveraging improvements in the tidal modelling framework that underpins the ITEM
191 modelling process. The tidal modelling used in ITEM v1.0 was constrained spatially into $1^\circ \times$
192 1° resolution image cells (approximately 110 x 110 km at the equator), with a single tidal
193 height assigned to the centre of each Landsat image based on its time of acquisition. This
194 spatially consistent image cell grid implicitly assumed that tidal heights did not vary across
195 the $1^\circ \times 1^\circ$ cell extent, and that a single modelled tide height per cell could adequately reflect
196 complex tidal dynamics operating at a range of spatial scales. This assumption resulted in
197 sometimes severe model discontinuities at some cell boundaries and poor modelling
198 performance in complex estuaries and other coastal areas characterised by high tidal flux
199 (Sagar et al., 2018, 2017). ITEM v2.0 was developed by replacing the spatially consistent
200 image cell grid with a multi-resolution tidal framework developed by Sagar et al. (2018). The
201 framework uses partitioning methods to allow spatial variability in the tidal model to drive the
202 size and locations of a Voronoi polygon mesh. The 306 resulting tidal modelling polygons
203 (Figure 1) are then used as analysis units for the ITEM modelling process, with tide height
204 predictions defined at the nodes of each Voronoi cell. We used the Oregon State University
205 Tidal Prediction Software (OTPS) TPX08 model (Egbert and Erofeeva, 2010, 2002) to
206 predict tide heights. OTPS tidal modelling has been used successfully for continental-scale
207 intertidal modelling applications in both Asia and Australia (Murray et al., 2012; Dhanjal-
208 Adams et al., 2016). The model consists of a multi-resolution bathymetric grid with a $1/6^\circ$
209 resolution ($\sim 18 \times 18$ km at the equator) solution in the global open ocean and a $1/30^\circ$ local
210 resolution ($\sim 4 \times 4$ km) solution to improve modelling in complex shallow-water environments,
211 and has been validated to ~ 12 cm root mean square error (RMSE) misfit against the
212 Australian Hydrographic Office AusTides tide gauge records (Rogers et al., 2017). The study
213 area for ITEM v2.0 and NIDEM has been extended to cover the Great Barrier Reef and the
214 entire Australian coastline, including Tasmania. The use of the multi-resolution tidal model
215 has produced significant improvements in the coverage and resolution of the relative
216 intertidal extents model, most notably in the offshore regions of northern Australia and the
217 Kimberley coast in north-western Australia.

218 Unfiltered absolute elevation

219 ITEM v2.0 details the relative extent of the intertidal zone at intervals of the observed tidal
220 range. As such, it provides topography of the exposed intertidal surface but not an absolute
221 elevation measure. To derive absolute elevations, we used the *find_contours* function from
222 *scikit.measure* (Van der Walt et al., 2014) to extract waterline contours (Figure 2b) along the
223 boundary of each of the ten percent tidal interval boundaries in ITEM v2.0 (Figure 2b). This

224 contour extraction method uses the ‘marching squares’ algorithm (Lorensen and Cline,
225 1987) to identify precise contour boundaries in a two-dimensional array by linearly
226 interpolating between adjacent pixel values. For each interval boundary, we computed the
227 median tidal height of the ensemble of all Landsat observations originally used to derive the
228 corresponding median composite NDWI layer, and assigned this height as the contour’s z-
229 value. To convert contours to continuous elevation data rasters, we first extracted x, y and z
230 point data for each contour vertex, and used these points as inputs for interpolation. We
231 used the *griddata* interpolation function from *scipy.interpolate* (Jones et al., 2014), and
232 selected the ‘linear’ interpolation method to ensure that interpolated elevation values
233 preserved the tidal interval boundaries of ITEM v2.0. This interpolation method computes a
234 Triangulated Irregular Network or Delaunay triangulation of the input data using the
235 Quickhull algorithm (Barber et al., 1996), before performing linear barycentric interpolation
236 on each triangle to estimate new values for each pixel (Figure 2c). We set the output
237 resolution of the interpolation to 25 x 25 m, producing two-dimensional elevation arrays that
238 matched the cell size and extent of the original ITEM v2.0 layers and input Landsat
239 observations. As elevations for the lowest and highest ITEM v2.0 intervals could not be
240 correctly interpolated because they had no lower or upper bounds, we constrained the
241 interpolated elevation arrays to the observed intertidal zone by masking out pixels located
242 within consistently inundated (ITEM v2.0 interval 0) and consistently non-inundated terrain
243 (interval 9). This resulted in a set of 306 ‘unfiltered’ intertidal elevation datasets with
244 elevations in metre units relative to modelled MSL (approximately equivalent to the
245 Australian Height Datum or AHD). To facilitate future re-analysis such as the application of
246 alternative interpolation methods, waterline contours were exported as shapefiles.

247 Filtered absolute elevation

248 The accuracy of intertidal elevation modelling approaches based on waterline extraction and
249 tidal modelling is dependent on the ability of a tidal model to correctly assign and sort
250 satellite observations by tidal height (Liu et al., 2013b; Sagar et al., 2017). This assumption
251 may not hold in areas that have undergone significant geomorphological change across the
252 30-year time series, or where modelled tidal heights differ from actual tidal heights due to
253 inherent model error (Ryu et al., 2008; Sagar et al., 2017). To identify potentially invalid
254 elevation values, we used a ‘confidence’ layer developed as part of ITEM v2.0. The ITEM
255 confidence layer is based on the per-pixel variance in NDWI values for the ensemble of
256 images used to produce each ten percent tidal interval composite. We used a conservative
257 maximum threshold of 0.25 NDWI standard deviation to mask out over 1980 km² of intertidal

258 pixels (5.5% of the total 'unfiltered' dataset) where tidal processes poorly explained
259 inundation patterns across the 30-year time series.

260

261 The robust median compositing method used to combine NDWI images in ITEM 2.0 ensured
262 that the input relative intertidal extent layers were relatively free of artefacts including
263 outliers, poorly removed cloud edges and sunglint that commonly affect coastal remote
264 sensing imagery (Sagar et al., 2017; White et al., 2014). However, composite layers
265 produced from multiple satellite observations can still be susceptible to artefacts in regions
266 with high cloud cover or fewer observations in the Landsat archive (Flood, 2013; White et al.,
267 2014; Roberts et al., 2017). For NIDEM, this typically manifested as pixels located either
268 inland of the coastal zone or in areas of deeper water incorrectly mapped as intertidal terrain
269 in data poor areas of the Australian coastline. To remove these artefacts, we restricted
270 NIDEM layers to a 50 m elevation range centred on MSL. This large range relative to the
271 maximum Australian tidal range of over 11 m (Solihuddin et al., 2016) was selected to
272 remove obvious false positives without eliminating true intertidal terrain. We used elevation
273 data from Australia's SRTM-derived 1 Second Digital Elevation Model (Gallant et al., 2010)
274 to mask out approximately 402 km² of terrain with elevations greater than 25 m above MSL
275 (1.1% of the total 'unfiltered' dataset). Bathymetry data from the national 250 m Australian
276 Bathymetry and Topography Grid (Whiteway, 2009) and the 30 m gbr30 and nhaus30 high-
277 resolution depth models for the Great Barrier Reef and Northern Australia (Beaman, 2018a,
278 2018b) were used to mask out pixels located at depths of greater than -25 m in all three
279 datasets. This removed over 18,325 km² of misidentified intertidal terrain (50.7% of the total
280 'unfiltered' dataset) which was largely concentrated (i.e. 9571 and 4574 km², or 26.5 and
281 12.7%) in two data-poor tidal modelling polygons located off the Archipelago of the
282 Recherche in southern Western Australia. All layers were reprojected to the resolution (25 x
283 25 m) and projection system (GDA94 Australian Albers, EPSG:3577) of the NIDEM layers
284 using bilinear resampling prior to masking. The resulting masked layers were exported as
285 "filtered" elevation datasets, while the combined mask (i.e. ITEM confidence, bathymetry and
286 elevation limits) was exported as "mask" layers to facilitate re-analysis through the
287 application of customised masking criteria.

288 Tidal range coverage

289 To evaluate the representativeness of NIDEM data compared to the full tidal range, we
290 compared the spread of tidal heights coincident with the input Landsat imagery against the
291 full range of modelled tide heights present within each tidal modelling polygon. We
292 calculated three indices: spread (the proportion of the full modelled tidal range observed by

293 Landsat), low tide offset (the proportion of the lowest tidal heights not observed by Landsat)
294 and high tide offset (the proportion of the highest tidal heights not observed by Landsat). The
295 variations in these indices in different regions relate to the sun-synchronous nature of
296 observations from satellites such as the Landsat series, and are discussed in the following
297 section.

298 Validation

299 To assess the accuracy of NIDEM, we validated 'filtered' elevations at multiple sites and
300 intertidal environments along the Australian coastline. We used the nationally-consistent
301 coastal 'Smartline' geomorphic and stability map (Sharples et al., 2009) to identify the
302 dominant intertidal landform type for each validation site. These landforms were summarised
303 into three distinct intertidal categories: sandy beaches (including sandy and mixed sand
304 beach and shores), tidal flats (including sand, mud and undifferentiated tidal flats) and rocky
305 reefs and shores (including hard bedrock shores). We obtained validation data from three
306 different elevation and bathymetry data sources: the DEM of Australia derived from LiDAR 5
307 Metre Grid (Geoscience Australia, 2015), point elevation data collected from Real Time
308 Kinematic (RTK) GPS surveys (Danaher and Collett, 2006; HydroSurvey Australia, 2009),
309 and 1.0 m resolution multibeam bathymetry surveys (Solihuddin et al., 2016). Validation
310 datasets were processed as described below and pooled across sample sites for each
311 intertidal environment type. We compared modelled (i.e. NIDEM) and observed (i.e.
312 validation) data using the *pandas* Python package (McKinney, 2011) by calculating RMSE
313 accuracy and two correlation coefficients (Pearson's and Spearman's). Pearson's correlation
314 was used to assess whether NIDEM accurately modelled absolute elevation by evaluating
315 the linear relationship between modelled and observed values. Spearman's correlation
316 assessed whether modelled elevations were monotonically related to validation elevations,
317 allowing us to evaluate if at a minimum the relative – not absolute – topography of the
318 intertidal zone was captured by NIDEM. For example, this could assess to what extent actual
319 low tide terrain was correctly identified as low tide terrain in NIDEM even if absolute
320 elevations from the tidal model were incorrect.

321 LiDAR validation data

322 The bare-earth LiDAR 5 Metre Grid covers over 245,000 km² of predominantly coastal
323 terrain across eastern and northern Australia with accuracy of better than 0.30 m (95%
324 confidence, AHD vertical datum; Geoscience Australia, 2015). However, the dataset has
325 sporadic coverage of the intertidal zone, with some coastal regions affected by elevation
326 discontinuities caused by aerial surveys flown at different tidal stages (e.g. Figure 3a). To

327 extract usable validation data for the intertidal zone in areas affected by these artefacts, we
328 developed a novel LiDAR point-cloud tidal tagging approach to identify non-inundated
329 intertidal terrain in the DEM. Fourteen validation sites (Figure 1) were identified within
330 randomly selected tidal modelling polygons based on the availability of extensive intertidal
331 terrain in both NIDEM and LiDAR datasets. LiDAR 5 Metre Grid data was extracted for each
332 of these sites and reprojected using average resampling to match the NIDEM resolution and
333 projection system with the *gdalwarp* image reprojection and warping utility (GDAL/OGR
334 contributors, 2018). For eight of the fourteen validation sites affected by tidal artefacts, we
335 used the *las2txt* tool from *LAStools* software (Isenburg, 2018) to extract a 1% sample of xyz
336 points and associated metadata from the .las format LiDAR point-cloud datasets used to
337 generate the LiDAR 5 Metre Grid (Figure 3b). For each extracted LiDAR point, we used the
338 OTPS tidal model (Egbert and Erofeeva, 2002, 2010) to compute a tidal height relative to
339 MSL based on the point's time of acquisition timestamp. By rasterising all points with z-
340 values (elevations) greater than the instantaneous tidal height at the time of LiDAR
341 acquisition (plus a 0.15 m buffer to account for point cloud noise), we produced a binary
342 mask representing non-inundated terrain in the LiDAR DEM. This mask was cleaned to
343 remove remaining noise by using the *scipy.ndimage* mathematical morphology
344 *binary_opening* and *binary_closing* tools (Jones et al., 2014). Binary opening removed
345 isolated pixels by 'eroding' (shrinking the data area by one pixel) and subsequently 'dilating'
346 (expanding the remaining data area by one pixel) the mask layer, while binary closing filled
347 gaps by first dilating then eroding the array (Serra, 1983). The resulting cleaned mask was
348 then used to extract intertidal validation data from the original LiDAR 5 Metre Grid (Figure
349 3c).

350 RTK GPS validation data

351 RTK GPS transect elevation survey data covering tidal flats at East Point in Mindal Bay,
352 Darwin and Moreton Bay, Queensland (Figure 1) were collected by HydroSurvey Australia
353 (2009) and Danaher and Collet (2006). Point data with elevations in AHD (stated vertical
354 accuracy of ± 0.02 m) from both surveys were rasterised to match the NIDEM resolution and
355 projection system by taking the average elevation value when multiple GPS points fell within
356 a single Landsat pixel.

357 Multibeam bathymetry validation data

358 Multibeam bathymetry validation data were obtained for five sites in the Buccaneer
359 Archipelago in the southern Kimberley region (Cockatoo Island, east Tallon Island, west
360 Tallon Island, Waterflow and Irvine/Bathurst Islands; Figure 1). The data consisted of 1 m
361 resolution gridded AHD reef elevations measured using an Odom ES3 multibeam echo

362 sounder with a Trimble RTX satellite subscription (± 0.02 m positioning accuracy; Solihuddin
363 et al., 2016). All multibeam data were resampled to the NIDEM resolution and projection
364 system using average resampling.

ACCEPTED MANUSCRIPT

365 Results and Discussion

366 In this study, we present an automated approach to generating satellite-derived elevation
367 data for over 15,387 km² of exposed intertidal sandy beaches and shores, tidal flats and
368 rocky shores and reefs across the entire Australian coastline (Bishop-Taylor et al., 2018;
369 Figure 4, 5). Intertidal elevations in metre units relative to modelled MSL ranged between -
370 5.57 m to +3.41 m, with the largest spread of elevations located in the macrotidal Kimberley
371 region in north-western Australia (7.69 m) and the central Queensland coast of eastern
372 Australia (4.58 m). Although previous studies have mapped the extent of the intertidal zone
373 both globally (Murray et al., 2018) and at continental-scale across Southeast Asia (Murray et
374 al., 2012) and Australia (Dhanjal-Adams et al., 2016; Sagar et al., 2017), to our knowledge
375 NIDEM represents the first continental-scale DEM of the intertidal zone.

376 Model performance across sandy beaches and shores

377 Elevation values from NIDEM agreed well with LiDAR 5 Metre Grid validation datasets
378 across sandy beach and shore intertidal environments. Validation elevations for 121,725
379 paired pixels pooled across five sites along the Australian coastline were strongly correlated
380 with NIDEM (Pearson's $\rho = 0.92$, Spearman's $\rho = 0.93$), resulting in a low RMSE of ± 0.41 m
381 which approached the vertical accuracy of the contributing LiDAR surveys (i.e. <0.30 m;
382 Figure 6a, Table 1). Our results compare favourably to more manual, non-automated
383 approaches to waterline delineation, including the construction of intertidal DEMs for a 1,267
384 km² portion of the Dongsha sandbank in China's Jiangsu Province using on-screen
385 digitisation of MODIS and Landsat imagery (Liu et al., 2013a, 2013b). The Dongsha
386 sandbank DEMs exhibited similarly strong correlations with LiDAR validation data ($R^2 =$
387 0.92), with vertical accuracies of between ± 0.45 - 0.62 m RMSE depending on the number of
388 input satellite images used to generate the DEMs. Tseng et al. (2017) achieved similar
389 correlations (Pearson's $\rho = 0.93$) and vertical accuracies (RMSE of ± 0.48 m) for tidal gauge-
390 based validation of a intertidal DEM produced for the Hsiang-Shan Wetland in Taiwan using
391 22 years of Landsat imagery, although this DEM covered a relatively small extent of 16 km².

392

393 Poor modelling results occurred at a single site near Robbins Island in north-western
394 Tasmania where accuracies were significantly lower (RMSE of ± 0.57 m) than the four other
395 sites assessed (≤ 0.34 m; Table 1). This result was driven by a set of outlying values where
396 NIDEM predicted low elevations between 0.0 to 0.5 m for an area of intertidal terrain with
397 actual elevations ranging from 1.0 to 2.0 m (Figure 6a). The Robbins Island site occurs on
398 the boundary of two large shallow tidal basins (Boullanger Bay and Big Bay) and the
399 intersection of three estuaries (the Duck, Montagu and Welcome Rivers), creating highly

400 variable and unpredictable tidal conditions (Spruzen et al., 2008; Donaldson et al., 2012).
401 This complex tidal regime challenges the application of any continental-scale tidal model,
402 especially given that the individual instantaneous modelled tide heights used to assign
403 elevations to waterlines are likely to rapidly decrease in accuracy with increasing distance
404 from a given modelling point (Donaldson et al., 2012; Bell et al., 2016). In this study, we
405 attempted to moderate the influence of spatially variable tidal conditions by adopting a multi-
406 resolution tidal modelling framework that allowed local complexity in tides to drive the scale
407 and boundaries of the model (Sagar et al., 2018). This minimised the distance between each
408 satellite image and the locations used to calculate tides, resulting in a closer match between
409 the tidal stage observed from space and the resulting attributed tide height. At the Robbins
410 Island site, however, the resulting automatically derived tidal modelling polygons dissected
411 Boullanger Bay in the west of the study site, causing an area of intertidal terrain within the
412 bay to be assigned tidal heights that were more appropriate for the western Tasmanian open
413 coast (see Appendix A1). Although this result highlights areas where the multi-resolution
414 tidal modelling framework used in this study could be improved, results for other sites
415 indicate that the approach provides a significant improvement over previous artefact-prone
416 continental-scale modelling frameworks which used a regular 1 x 1 degree grid to assign tide
417 heights to imagery (Sagar et al., 2018).

418 Model performance across tidal flats

419 We compared the performance of NIDEM across 99,506 pixels of tidal flat terrain at nine
420 LiDAR 5 Metre Grid and RTK GPS survey sites across northern and southern Australia
421 (Figure 6b, Table 1). Although overall accuracies were high and consistent with sandy beach
422 and shore sites (RMSE of ± 0.39 m), tidal flats exhibited slightly lower correlations overall
423 (Pearson's $\rho = 0.78$, Spearman's $\rho = 0.81$). This result was expected given two interacting
424 characteristics of tidal flat environments: their extensive, low-slope morphology and
425 dynamism. Tidal flats are known to be highly variable, and can undergo significant
426 geomorphic change in response to tidal processes and changes in sediment flux (Mason et
427 al., 2010; Chen et al., 2016). Even small vertical changes in elevation in these gently sloping
428 environments can produce large horizontal shifts in waterline locations (e.g. a 0.1 m change
429 in elevation on a 1:500 slope tidal flat would result in a 50 m horizontal discrepancy in
430 waterline position, equivalent to two Landsat pixels; Mason et al., 1995; Zhao et al., 2008).
431 This presented a particular challenge to our composite-based approach, as coastal change
432 at any point across our 30-year time-series would invalidate or reduce the accuracy of our
433 waterline-derived modelled elevations. Previous studies have generated intertidal DEMs
434 based on shorter temporal extents to reduce the influence of coastal change (e.g. Zhao et

435 al., 2008; Liu et al., 2013b), however these approaches risk reducing the overall accuracy of
436 modelled elevations by limiting available satellite observations and increasing the relative
437 influence of natural variability and noise. To minimise the impact of geomorphic change
438 while maximising our use of the Landsat archive, our approach used NDWI variance to mask
439 individual pixels where tidal modelling poorly explained patterns of inundation (i.e. ITEM 2.0
440 confidence; Sagar et al. 2017). Although this approach effectively removed areas of
441 significant coastal change, the choice of a single universal masking value (i.e. 0.25 NDWI
442 standard deviation) unavoidably preserved areas of intertidal terrain subject to subtler, long-
443 term geomorphic change. In these areas, NIDEM represents median or 'typical' elevation
444 conditions across the 30-year time series.

445

446 Validation results for tidal flat environments revealed a distinct lack of modelled elevation
447 data for the upper portion of the tidal range (e.g. between 0.5 and 1.3 m AHD; Figure 6b). In
448 tidal flats, the elevation zone above mean sea level is typically occupied by coastal wetlands
449 including mangroves (Bunt et al., 1985; see Appendix A2). Although these vegetated
450 intertidal communities are regularly inundated by tidal flows, patterns of inundation are
451 difficult to observe from satellites due to the presence of dense canopy cover. This was
452 particularly true for the NDWI index used to detect water in our model, which intentionally
453 differentiates between open water and vegetated features based on their low and high
454 reflectance of NIR radiation respectively (McFeeters, 1996). Although areas of exposed tidal
455 flat terrain located behind mangroves were accurately modelled by NIDEM across our nine
456 validation sites (i.e. areas above 1.3 m AHD in Figure 6b), vegetative resistance to flowing
457 water in mangrove, saltmarsh and other coastal wetland communities can cause significant
458 hydrodynamic attenuation in tidal flow (Rodríguez et al., 2017; Montgomery et al., 2018).
459 This would affect the spatial distribution of extracted waterlines by creating lags between
460 tidal conditions and patterns of observed water. Due to these issues, caution should be
461 applied when interpreting elevation values for intertidal regions on the landward side of
462 coastal wetlands (e.g. Appendix A2), or other environments such as estuaries or areas
463 influenced by artificial hydraulic structures where tidal flows may be similarly modified or
464 restricted (Williams and Watford, 1997; Rodríguez et al., 2017).

465 Model performance across rocky shores and reefs

466 Although NIDEM produced accurate modelled elevations in sandy beaches and tidal flat
467 environments, results were less accurate within rocky shore and reef environments.
468 Modelled elevations ($n = 2299$) had a low Pearson's correlation of 0.46 and a high RMSE of
469 ± 2.98 m vertical accuracy compared to LiDAR 5 Metre Grid and multibeam bathymetry data

470 for seven validation sites (Figure 6c, Table 1). Spearman's correlation was higher at 0.79,
471 indicating that NIDEM largely captured the relative – but not absolute – topography of the
472 surveyed sites. This poor result was driven by validations across five Buccaneer Archipelago
473 reef sites within the southern Kimberley region, including one site (Cockatoo Island) where
474 NIDEM elevations were negatively correlated with multibeam bathymetry (Pearson's and
475 Spearman's ρ of -0.26 and -0.19; Table 1). The fringing reefs of the Buccaneer Archipelago
476 are exposed to an extreme and dynamic tidal regime, including the largest tidal range of any
477 coral reef system (approaching 11 m), with strong tidal currents that can exceed 18 km/h
478 (Purcell, 2002; Solihuddin et al., 2016). Of particular relevance to the NIDEM approach,
479 Lowe et al. (2015) observed significant asymmetry in tidal patterns on Tallon Island (one of
480 the sites included in the NIDEM validation), with the shallow, elevated intertidal reef platform
481 rapidly inundating over a short ~2 hour period during flood tides, before draining slowly over
482 ~10 hours during ebb tides. The presence of 'trapped' water on the reef platform for
483 extended periods caused areas of shallow exposed reef to appear as permanently inundated
484 terrain in the ensemble of input Landsat observations, and violated the assumptions of the
485 input ITEM model by causing modelled tidal heights to become unsynchronised from actual
486 water levels. Our results indicate that satellite-derived intertidal DEMs such as NIDEM are
487 unlikely to produce accurate elevations in regions that exhibit significant unaccounted-for
488 tidal asymmetry, or where the resolution or local accuracy of the tidal models used to assign
489 tide heights is low. Increasing the accuracy of estimated tide heights in these locations will
490 likely require accounting for finer-scale bathymetry and substrate conditions using locally
491 specified hydraulic modelling (e.g. Lowe et al. 2015) that would be challenging to apply at
492 the continental-scale. Future work should focus on developing additional methods for
493 quantifying local tidal asymmetry and poor tidal modelling performance so that the accuracy
494 and validity of satellite-derived intertidal DEMs can be quantitatively assessed for each pixel
495 of intertidal terrain.

496 Potential of continental-scale intertidal elevation modelling

497 Our results demonstrate that satellite-derived elevation models based on waterline extraction
498 can approach the accuracy of LiDAR for modelling the topography of tidal flats and sandy
499 beach and shore environments. The NIDEM approach is particularly suitable for remote
500 areas of inaccessible coastline (e.g. northern Australia) where higher-resolution approaches,
501 such as shallow-water multibeam bathymetry or airborne bathymetric LiDAR, would be cost
502 prohibitive or impractical. By providing an important 'missing link' between existing medium
503 resolution terrestrial topographic and marine bathymetric datasets, we anticipate elevation
504 data from NIDEM will contribute to unified coastal terrain models that combine best-available

505 topography and bathymetry datasets into single continuous ‘topobathy’ datasets (Hogrefe et
506 al., 2008). Examples are the ntha30 depth model for Northern Australia (Beaman, 2018b)
507 and the gbr30 depth model for the Great Barrier Reef (Beaman, 2018a) used to test the
508 inclusion of NIDEM as source elevation data (Figure 7). NIDEM data fills in the shallow reef
509 flats around islands and sand bars within river channels, while subtly reducing the stepping
510 effect across the land-sea interface. NIDEM could thus provide coastal managers with near-
511 seamless elevation data extending from inland to the ocean floor, and support a holistic
512 approach to understanding the physical and ecological processes influencing the coastal
513 zone. This may include providing valuable baseline elevation data for predicting the impact
514 of coastal hazards such as storm surges or tsunami inundation (e.g. Skinner et al., 2015;
515 Smolders et al., 2015), investigating mechanisms of coastal erosion and sediment transport
516 (Ryu et al., 2001, 2008; Hsu et al., 2013; Gharibreza et al., 2014), or improving modelling of
517 sea-level rise under future climate change scenarios (Galbraith et al., 2002; Thorner et al.,
518 2014). Access to accurate intertidal elevation data is also critical for studying and conserving
519 coastal ecosystems, particularly given the important role intertidal topography and tidal
520 dynamics play in regulating environmental stress and spatial patterns of species richness,
521 abundance and productivity (Scrosati et al., 2011; Valdivia et al., 2011). The outputs from
522 NIDEM facilitate whole-of-landscape approaches to ecological modelling and three-
523 dimensional habitat mapping in the intertidal zone that are not artificially restricted to either
524 the marine or terrestrial domain.

525
526 A key advantage of our continental-scale approach to intertidal elevation modelling was
527 using composite layers to identify the typical location of the waterline at various tidal heights.
528 Intertidal zones exhibit considerable natural variability in the location of the waterline
529 between identical tides or during ebb and flow stages (Ryu et al., 2001; Boak and Turner,
530 2005; Li and Gong, 2016). Wave run-up or the effect of wind can affect the location of
531 waterlines by tens of meters on low sloping beaches or flats (Thieler and Danforth, 1994),
532 while long-term sea-level variation, seasonal influences or storm surge events can drive
533 additional unpredictable variability (Boak and Turner, 2005; García-Rubio et al., 2015).
534 Recent long-term shoreline trend studies have shown that combining multiple observations
535 into composite layers can effectively isolate these factors, and allow waterline contours to be
536 extracted that can be up to twice as spatially accurate as the resolution of the input satellite
537 imagery (Almonacid-Caballer et al., 2016; Hagenaars et al., 2018). Generating median
538 composites at ten percent increments of the tidal range allowed us to both reduce sources of
539 natural variability and extract waterline contours that were most representative of the
540 shoreline position across the full range of observed tidal conditions (Almonacid-Caballer et
541 al., 2016). Using a robust central tendency median compositing method based on good

542 quality Landsat pixel observations combined with an elevation and bathymetry filtering step
543 also greatly reduced sensor artefacts and noise, including false positives in data-poor
544 deeper ocean areas affected by sunlint or clouds. Issues with noise persist in some areas
545 close to the coast, including the Archipelago of the Recherche in southern Western
546 Australia, Port Phillip Bay in Victoria, and the south-eastern coast of Tasmania and King
547 Island (Figure 1). However, across most of the Australian coastline these approaches
548 effectively eliminated the need for manually-derived masks (e.g. Chen and Chang, 2009;
549 Murray et al., 2012) or the subjective manual selection of clear scenes (Boak and Turner,
550 2005). This allowed us to leverage the full Landsat archive, and facilitated the automated
551 extraction of waterline contours at a scale that would be impractical based on manual
552 waterline digitisation (e.g. Zhao et al., 2008). Importantly, this automated approach improves
553 reproducibility, allowing NIDEM to be improved over time as new Landsat observations are
554 added to the DEA platform. To facilitate re-analysis, NIDEM is released in both a 'filtered'
555 and 'unfiltered' version, allowing users to modify or apply custom filtering to the raw data
556 depending on their application.

557 Limitations and future work

558 The complex behaviour of tides mean that a sun synchronous sensor like Landsat does not
559 observe the full range of the tidal cycle at all locations (Eleveld et al., 2014; Parke et al.,
560 1987). To date, however, few studies modelling the extent and topography of the intertidal
561 zone have addressed issues of tidal bias (e.g. Murray et al., 2012; Chen et al., 2016; Tseng
562 et al., 2017), with the remainder implicitly assuming that satellite observations of the
563 coastline were representative of the full local tidal range. While biases in the proportion of
564 the tidal range observed do not affect the accuracy of absolute elevation models like NIDEM,
565 they can prevent models from providing elevation data for areas of the intertidal zone
566 exposed or inundated at the extremes of the tidal range. This risks giving misleading insights
567 into the true extent of the intertidal zone, and reduces the comparability of upper and lower
568 elevations at different locations. The portion of the tidal cycle observed by a sun
569 synchronous sensor can be estimated using a tidal model shown in Figure 8. Across the
570 Australian continent, both the overall spread of the observed tidal range compared to the full
571 tidal range (Figure 8a) and offsets in this proportion relative to the lowest and highest tidal
572 extremes (Figure 8b, c) varied greatly, even across relatively small distances in areas of
573 rapid tidal flux. This evaluation of the observed tidal range at a particular location provides
574 valuable information to users about the 'fitness for purpose' of NIDEM at a given location for
575 their specific application. We strongly recommend that future regional-, continental- or
576 global-scale intertidal zone analyses using EO data consider potential biases associated

577 with the representativeness of their input data relative to the full tidal range. This would serve
578 as an important first step to obtaining a better understanding of how processes driving
579 intertidal variability affect remote sensing analyses in the intertidal zone.

580

581 Liu et al. (2013b) performed a quantitative assessment of the factors influencing the
582 accuracy of intertidal DEMs, finding that overall DEM accuracy was strongly correlated with
583 the number of available input satellite observations. This increase in accuracy was driven
584 largely by the spatial coverage of waterline contours relative to total intertidal extent, with
585 higher densities of waterline contours leading to reduced RMSE. Interpolation error
586 represents a key source of uncertainty in waterline modelling approaches, with low contour
587 densities increasing the proportion of the study area requiring interpolation (Mason et al.,
588 2001; Liu et al., 2013b). The NIDEM approach based on tenth percentile tidal composites
589 can produce relatively large spacing between waterline contours compared to waterlines
590 digitised from individual observations, particularly in extensive shallow intertidal areas with
591 low topographic relief (Mason et al., 2001). Rather than combining tidally tagged imagery at
592 constant ten percent intervals of the tidal range, future work could develop an adaptive
593 approach to composite generation tailored to the local availability of high quality satellite
594 observations. This may result in a smaller number of higher quality tidal composites in areas
595 with few clear observations, and a denser collection of tidal composites in areas with
596 abundant clear observations throughout the 30-year time-series. By increasing the density of
597 extracted waterline contours, this adaptive approach would improve the ability of the DEM to
598 resolve finer-scale topographic features, and potentially allow high quality elevation
599 estimates to be produced using shorter temporal extents. This may facilitate the comparison
600 of DEMs from different temporal epochs to track and volumetrically estimate rates of coastal
601 change (e.g. Ryu et al., 2008; Mason et al., 2010). This could be a particularly powerful
602 approach for modelling the coastal zone if combined with additional sources of earth
603 observation data available from satellites, such as the European Space Agency's Sentinel-
604 2A and 2B, with a high revisit frequency compared to Landsat (approximately 5 days
605 compared to 14 days; Drusch et al., 2012).

606 Conclusion

607 In this study, we have presented an automated approach to modelling the elevation of the
608 intertidal zone based on a 30-year time series archive of Landsat remote sensing data and a
609 multi-resolution tidal modelling framework. The resulting NIDEM dataset is to our knowledge
610 the first continental-scale elevation model of the exposed intertidal zone, and provides an

611 unprecedented three-dimensional representation of Australia's tidal flats, sandy beaches and
612 shores, and rocky shores and reef environments at 25 m spatial resolution. NIDEM is based
613 on freely available EO data and open-source software, making it directly applicable to any
614 tidally influenced coastal environment globally. Future work will focus on integrating our
615 approach with higher spatial and temporal resolution sources of EO data (e.g. Sentinel 2),
616 and developing adaptive approaches to waterline contour extraction that will maximise the
617 tidal resolution of the model based on the local availability of high quality satellite
618 observations. This could enable modelling and comparison of finer-scale intertidal
619 topographic features across time and at the continental-scale.

620 Data availability

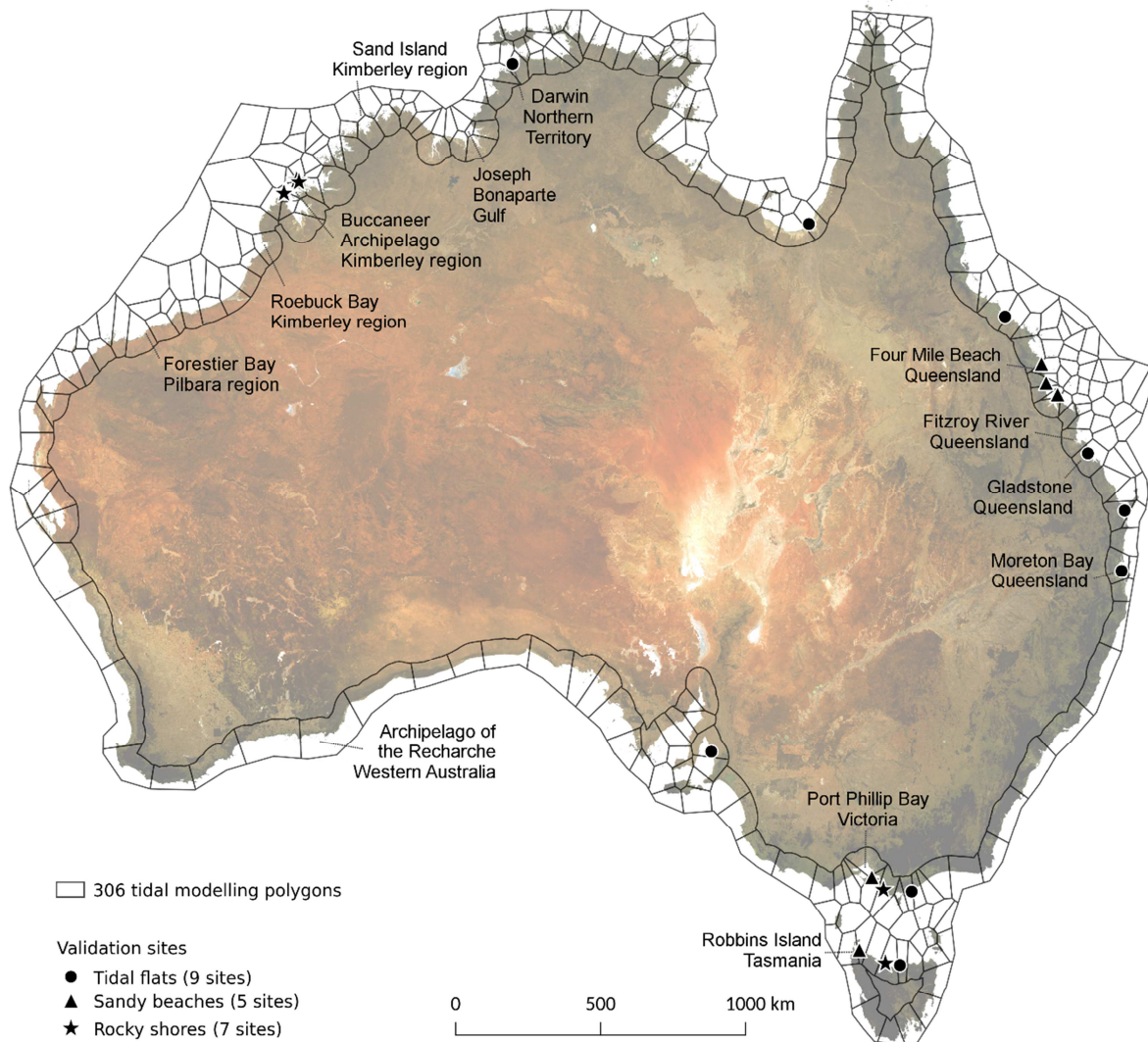
621 The datasets generated in this study (Bishop-Taylor et al., 2018) and additional metadata
622 can be accessed online (<http://www.ga.gov.au/dea/products>) and at the following persistent
623 links: NIDEM 1.0 (<http://dx.doi.org/10.26186/5c4fc06a79f76>) and ITEM 2.0
624 (<http://dx.doi.org/10.4225/25/5a602cc9eb358>). Code used to generate NIDEM is available in
625 the following repository: <https://github.com/GeoscienceAustralia/nidem>

626 Acknowledgements

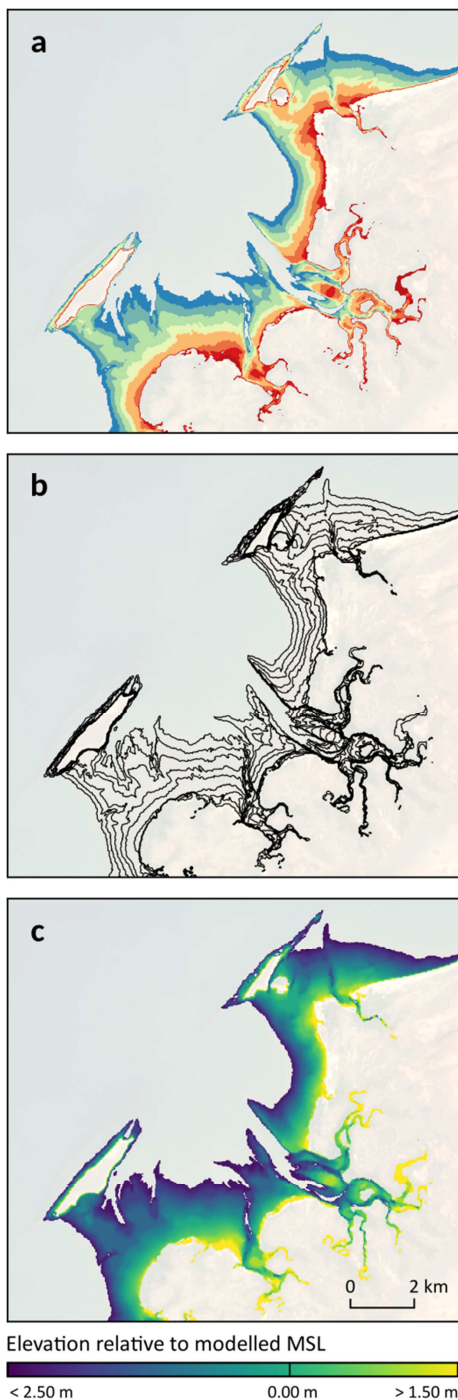
627 The authors would like to thank R. Nanson, F. Yuan, T. Dhu and two anonymous reviewers
628 for their valuable and constructive comments and suggestions. We thank the individuals and
629 organisations that provided validation data for this study. RTK GPS data used in Darwin
630 Harbour, NT was provided by HydroSurvey Australia, with the permission of GHD and Power
631 & Water Corporation, NT. RTK GPS data used in Moreton Bay, QLD was provided by Tim
632 Danaher, NSW Office of Environment and Heritage. Multibeam bathymetry data over the
633 Kimberley reefs was provided by M. O'Leary at Curtin University, WA. We thank C. Burton,
634 S. Chua, A. Haiblen, A. Lem, B. Moushall, B. Stepin and S. Wong for assisting with field
635 validation. This research was undertaken with the assistance of resources from the National
636 Computational Infrastructure (NCI) High Performance Data (HPD) platform, which is
637 supported by the Australian Government. This paper is published with the permission of the
638 Chief Executive Officer, Geoscience Australia.

639 **Figures**

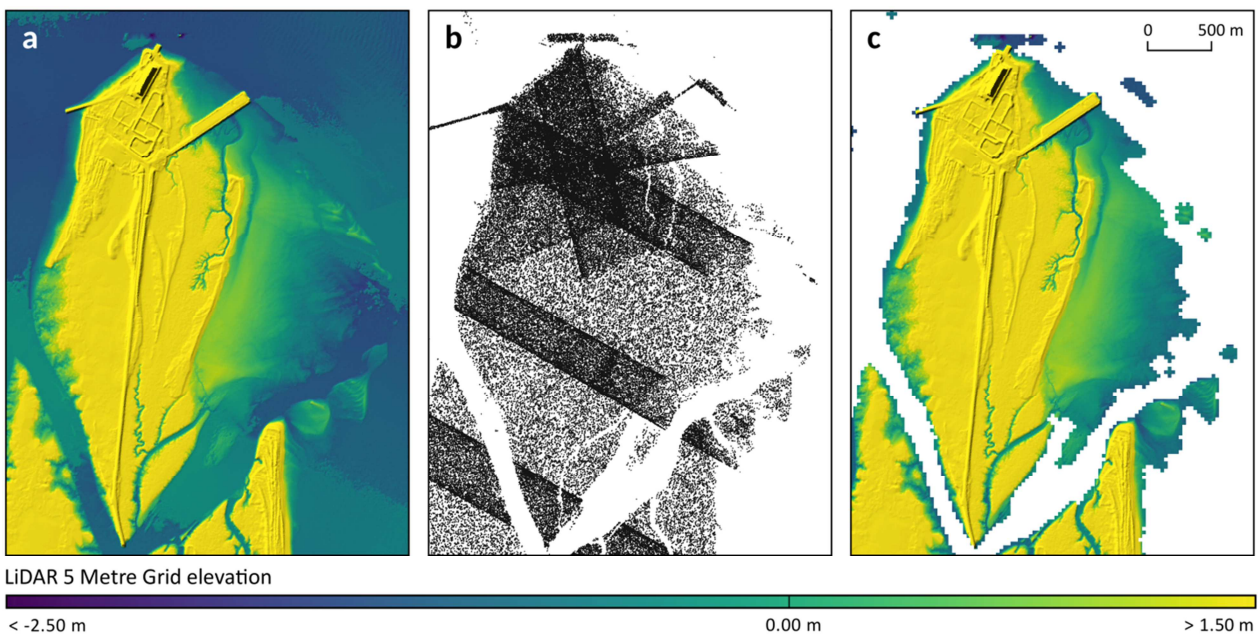
640 Figure 1. Map of the continental-scale Australian study area, showing the location of the 306
 641 tidal modelling polygons and validation sites for tidal flats (9 sites; circles), sandy beaches
 642 and shores (5 sites; triangles), and rocky shores and reefs (7 sites; stars). Labels highlight
 643 locations referred to in this work. Image underlay is a composite of all Landsat 8 satellite
 644 observations across Australia (Roberts et al., 2017).



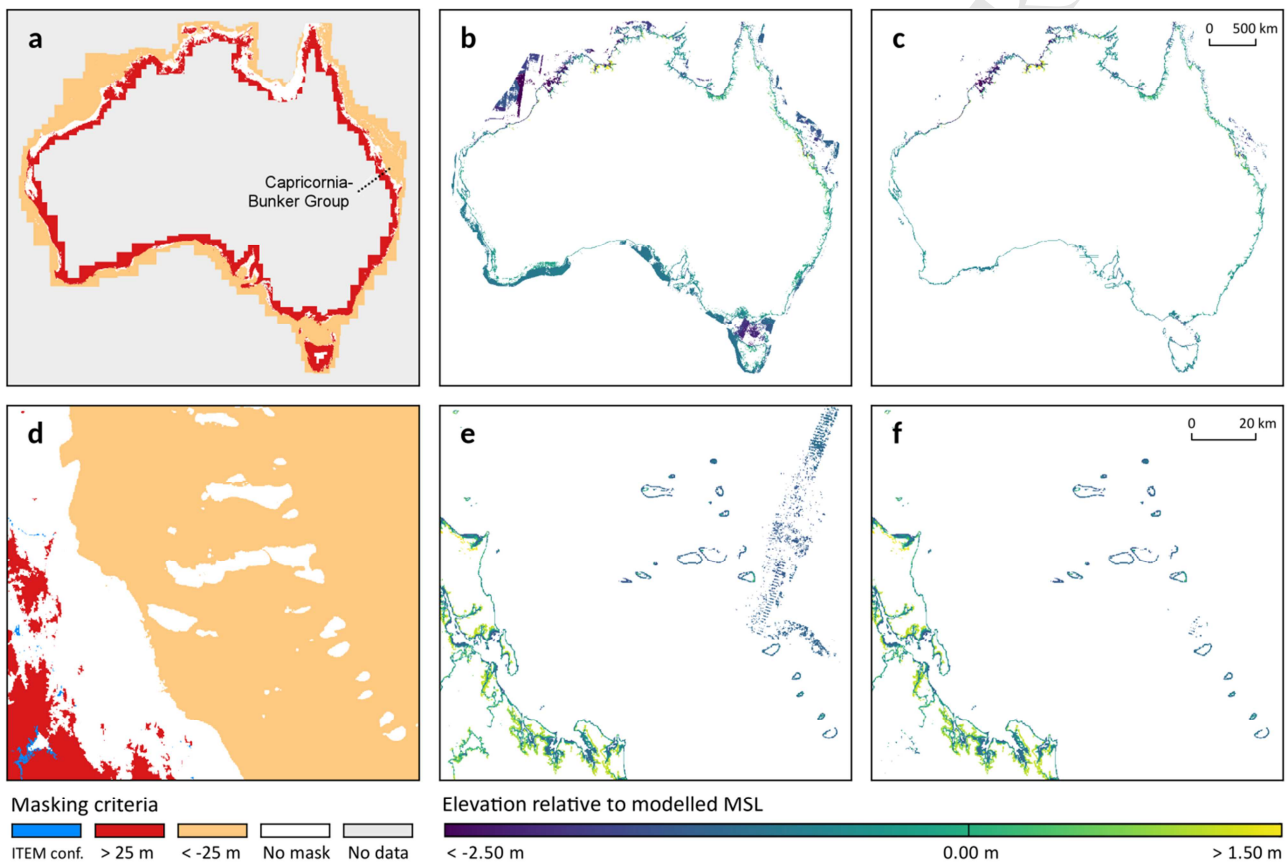
645 Figure 2. The process followed to extract and interpolate waterline contours for NIDEM for
646 an example area (Forestier Bay in the Pilbara region of Western Australia). Boundaries of
647 each (a) ten percent interval of the observed tidal range from ITEM v2.0 (colours from blue
648 to red indicate pixels inundated at increasingly high tide) were used to (b) extract contours
649 depicting the typical location of the land-water boundary across the 30-year Landsat time
650 series. These contours were assigned the median of all modelled tide heights attributed to
651 the ensemble of Landsat images used to generate each tidal interval. The resulting tidally-
652 tagged contours were used to generate (c) continuous elevation surfaces using triangulated
653 irregular network (TIN) interpolation.



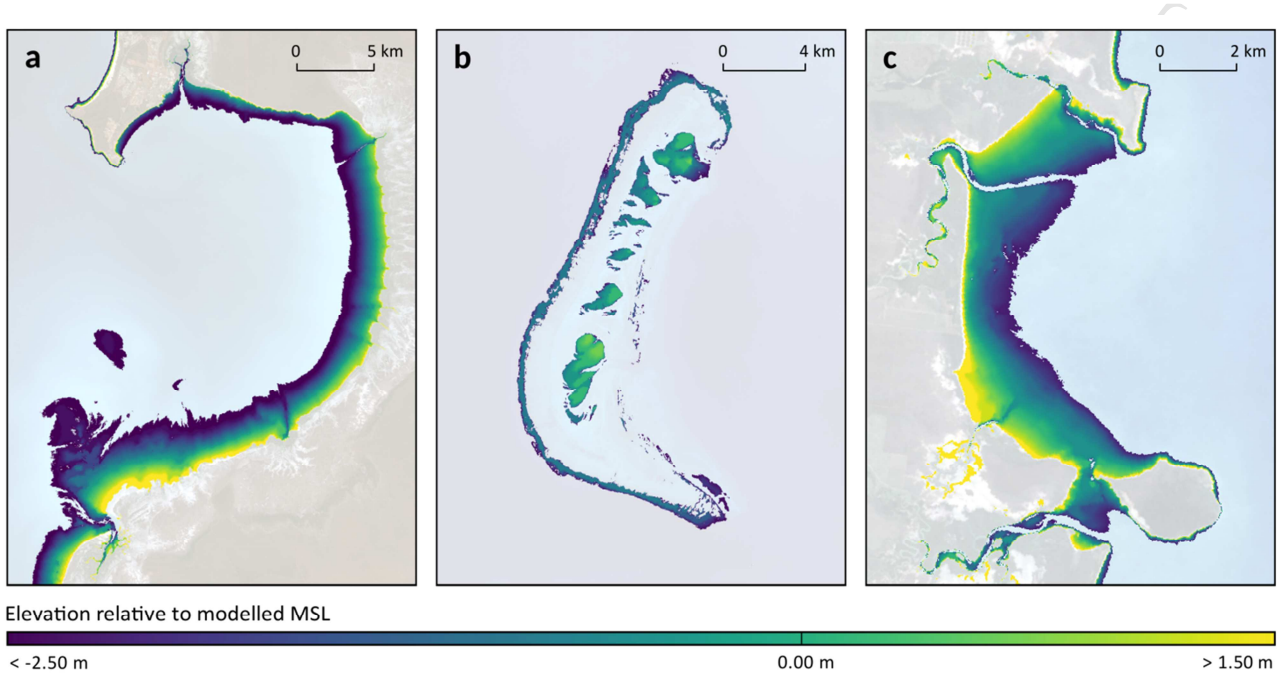
654 Figure 3. The process followed to extract usable validation data for the intertidal zone from
655 the (a) bare-earth LiDAR 5 Metre Grid dataset (Geoscience Australia, 2015) for an example
656 area affected by tidal-stage artefacts (Gladstone in central Queensland; dark colours
657 indicate greater depth). For each validation site, (b) xyz LiDAR point clouds were extracted
658 and tagged with tidal heights using the OTPS tidal model for the exact moment each point
659 was acquired. Tidally tagged points located above the water level at the time of LiDAR
660 acquisition were rasterized and used to produce a mask indicating the location of (c) non-
661 inundated intertidal terrain in the LiDAR DEM.



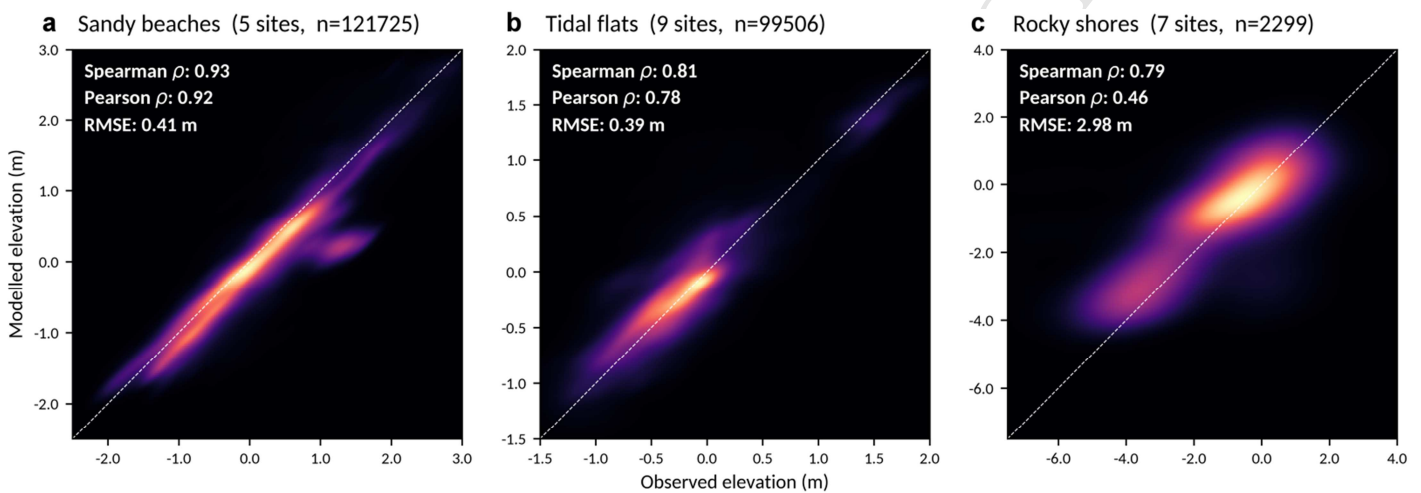
662 Figure 4. The output NIDEM layers at continental-scale (top row; aggregated to 2500 m pixel
 663 size for visualisation) and local-scale (bottom row; focused on the Capricornia-Bunker Group
 664 of reefs in central Queensland). The NIDEM 'mask' layer (a, d) highlights pixels flagged as
 665 exhibiting poor tidal model performance or significant geomorphic change across the 30-year
 666 time series based on the ITEM confidence layer (blue), pixels located above 25 m elevation
 667 (red) or pixels located below -25 m depth (orange). The effect of applying this mask can be
 668 seen by comparing the NIDEM 'unfiltered' layer (b, e) against the NIDEM 'filtered' layer (c, f)
 669 which was cleaned by masking by NIDEM 'mask'.



670 Figure 5. Examples of the 'filtered' NIDEM intertidal elevation data, including (a) Roebuck
671 Bay and (b) Sand Island in the Kimberley region of north-western Western Australia, and (c)
672 Four Mile Beach in the Isaac region of central Queensland.

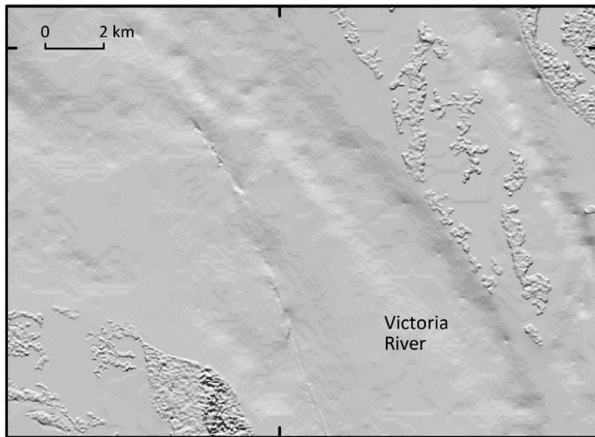


673 Figure 6. Validation results for NIDEM intertidal elevation compared across (a) five sandy
674 beach and shore sites, (b) nine tidal flat sites, and (c) seven rocky shore and reef sites.
675 Modelled (NIDEM 'filtered' elevations) and observed (validation) datasets are compared as
676 density heatmaps with associated correlation coefficients (Spearman and Pearson
677 correlation) and root mean square error (RMSE). Validation data was sourced from the
678 LiDAR 5 Metre Grid (Geoscience Australia, 2015), Real Time Kinematic (RTK) GPS surveys
679 from Darwin, Northern Territory (HydroSurvey Australia, 2009) and Moreton Bay,
680 Queensland (Danaher and Collett, 2006), and 1.0 m resolution multibeam bathymetry
681 surveys across the southern Kimberley region, Western Australia (Solihuddin et al., 2016).
682

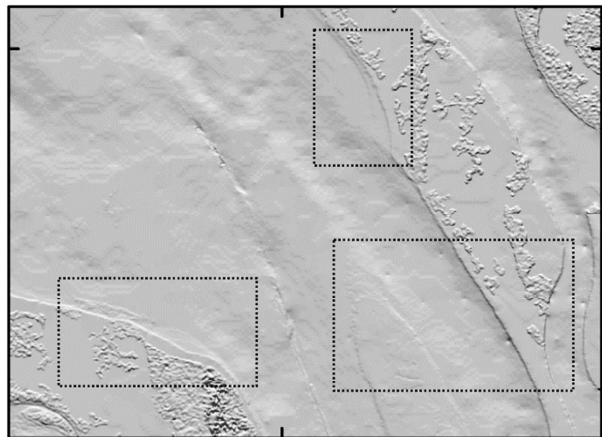


683 Figure 7. Hillshaded ntaus30 depth model for Northern Australia (Beaman, 2018b) showing
684 the Joseph Bonaparte Gulf and Victoria River area (a) before and (b) after the inclusion of
685 NIDEM; hillshaded gbr30 depth model for the Great Barrier Reef (Beaman, 2018a) showing
686 the Fitzroy River area of central Queensland (c) before and (d) after NIDEM. Note the
687 NIDEM data subtly improves the stepping effect across the land/ocean interface and helps
688 fill in the shallow reef flats around the islands and sand bars, resulting in better-defined river
689 channels.
690

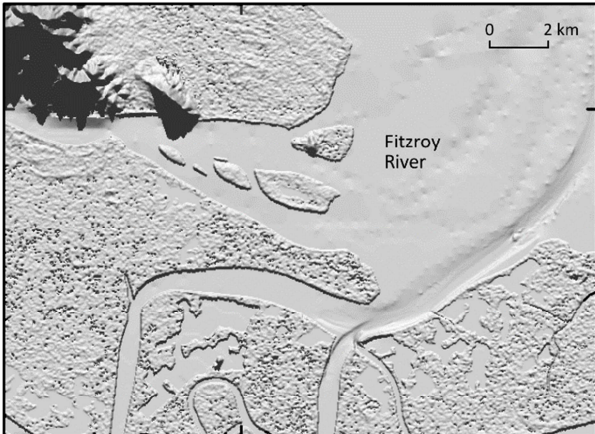
a Joseph Bonaparte Gulf: before



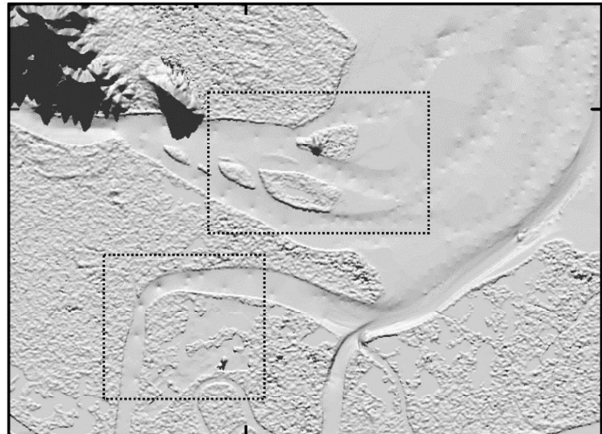
b Joseph Bonaparte Gulf: after



c Fitzroy River: before

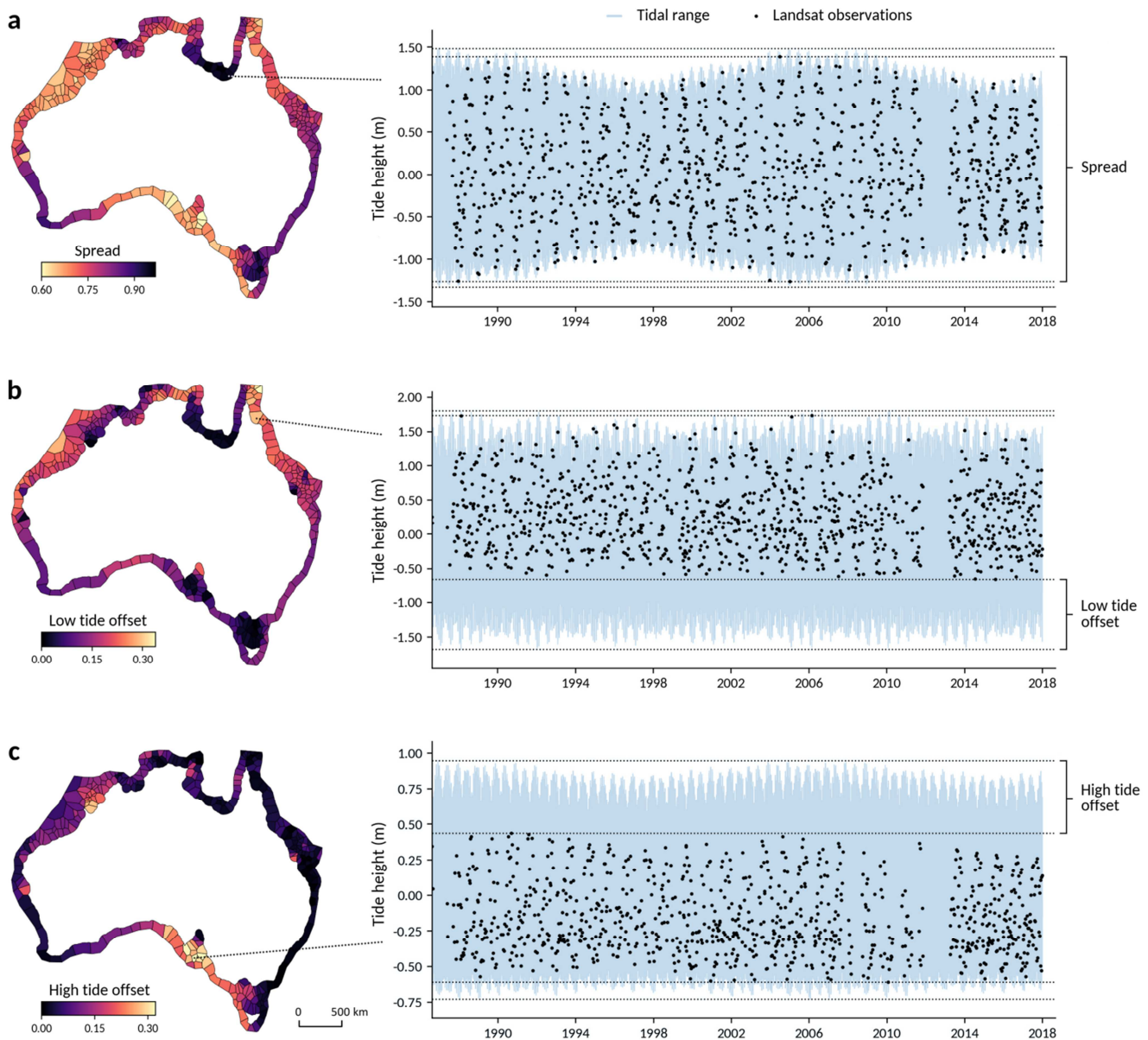


d Fitzroy River: after



691
692

693 Figure 8. The distribution of Landsat observations relative to the full tidal range. Light colours
 694 in the left panel indicate poor coverage of the tidal range by Landsat: light colours in (a)
 695 indicate polygons where Landsat observed a small ‘spread’ calculated as a proportion of the
 696 full tidal range. Light colours in (b) and (c) represent polygons where Landsat observations
 697 were biased away from low or high tides respectively. For example, a polygon with a spread
 698 of 0.7, an high tide offset of 0.05 and a low tide offset of 0.25 indicates that Landsat
 699 observed 70% of the tidal range, but did not image the highest 5% or lowest 25% of tide
 700 heights.



702 Tables

703 Table 1. Sites used for validating NIDEM 'filtered' intertidal elevation data, including LiDAR
 704 data from the DEM of Australia derived from LiDAR 5 Metre Grid (Geoscience Australia,
 705 2015) for 14 sites, elevation data collected from Real Time Kinematic (RTK) GPS surveys in
 706 Darwin, Northern Territory (HydroSurvey Australia, 2009) and Moreton Bay, Queensland
 707 (Danaher and Collett, 2006), and 1.0 m resolution multibeam bathymetry surveys for five
 708 sites in the southern Kimberley region, Western Australia (Solihuddin et al., 2016).
 709

Validation site	Upper left extent	Lower right extent	Intertidal type	Validation type	N	Spearman's ρ	Pearson's ρ	RMSE
Robbins Island	144.77569 E 40.67712 S	145.05675 E 40.80737 S	Sandy beach	Lidar	39142	0.67	0.78	0.57
Isaac	149.41409 E 21.70398 S	149.49239 E 21.84647 S	Sandy beach	Lidar	33756	0.98	0.97	0.29
Mackay	149.18434 E 21.13746 S	149.24215 E 21.24583 S	Sandy beach	Lidar	31863	0.96	0.94	0.34
Western Port	145.26148 E 38.38818 S	145.35062 E 38.43080 S	Sandy beach	Lidar	8341	0.92	0.91	0.18
Rockhampton	149.88750 E 22.06129 S	149.93865 E 22.14870 S	Sandy beach	Lidar	8077	0.96	0.95	0.33
North Adelaide	138.33472 E 34.56679 S	138.44901 E 34.68063 S	Tidal flat	Lidar	31267	0.69	0.38	0.5
Fraser	152.87081 E 25.50751 S	152.93960 E 25.60194 S	Tidal flat	Lidar	20553	0.76	0.81	0.31
Kaurumba	140.74169 E 17.41546 S	140.91024 E 17.51980 S	Tidal flat	Lidar	15217	0.92	0.88	0.27
Whitsunday	147.68246 E 19.77447 S	147.79755 E 19.84846 S	Tidal flat	Lidar	13707	0.92	0.96	0.19
Launceston	146.73713 E 41.04967 S	146.83075 E 41.12098 S	Tidal flat	Lidar	8029	0.87	0.88	0.33
Shoal Inlet	146.73026 E 38.65132 S	146.80500 E 38.69423 S	Tidal flat	Lidar	5630	0.77	0.7	0.3
Gladstone	151.26893 E 23.84394 S	151.33706 E 23.89089 S	Tidal flat	Lidar	4699	0.88	0.78	0.66
Darwin	130.78231 E 12.43566 S	130.85607 E 12.37220 S	Tidal flat	RTK GPS	274	0.93	0.9	0.63
Moreton Bay	153.03747 E 27.51057 S	153.23696 E 27.27759 S	Tidal flat	RTK GPS	130	0.86	0.87	0.17
Ulverstone	146.08124 E 41.11277 S	146.11576 E 41.12340 S	Rocky shore	Lidar	575	0.89	0.91	0.46
Kilcunda	145.44656 E 38.54480 S	145.48469 E 38.55914 S	Rocky shore	Lidar	323	0.63	0.49	0.61
East Tallon	123.12726 E 16.40046 S	123.14075 E 16.41921 S	Rocky shore	Multibeam	557	0.54	0.6	1.22
Bathurst and Irvine	123.51438 E 16.02877 S	123.56828 E 16.05869 S	Rocky shore	Multibeam	443	0.58	0.22	6.53
Tallon west	123.11392 E 16.40050 S	123.12354 E 16.41947 S	Rocky shore	Multibeam	283	0.8	0.54	0.86
Waterflow	123.06432 E 16.42213 S	123.08308 E 16.43144 S	Rocky shore	Multibeam	85	0.86	0.59	1.85
Cockatoo Island	123.59018 E 16.08976 S	123.60608 E 16.10020 S	Rocky reef	Multibeam	33	-0.26	-0.19	0.46

710 **References**

- 711 Almonacid-Caballer, J., Sánchez-García, E., Pardo-Pascual, J.E., Balaguer-Beser, A.A.,
712 Palomar-Vázquez, J., 2016. Evaluation of annual mean shoreline position deduced
713 from Landsat imagery as a mid-term coastal evolution indicator. *Marine Geology* 372,
714 79–88.
- 715 Banks, S.A., Skilleter, G.A., Possingham, H.P., 2005. Intertidal habitat conservation:
716 identifying conservation targets in the absence of detailed biological information.
717 *Aquatic Conserv: Mar. Freshw. Ecosyst.* 15, 271–288.
718 <https://doi.org/10.1002/aqc.683>
- 719 Barber, C.B., Dobkin, D.P., Huhdanpaa, H., 1996. The quickhull algorithm for convex hulls.
720 *ACM Transactions on Mathematical Software (TOMS)* 22, 469–483.
- 721 Barbier, E.B., Acreman, M., Knowler, D., 1997. Economic valuation of wetlands: a guide for
722 policy makers and planners. Ramsar Convention Bureau, Gland, Switzerland.
- 723 Beaman, R.J., 2018a. High-resolution depth model for the Great Barrier Reef - 30 m [WWW
724 Document]. Geoscience Australia. URL
725 <http://pid.geoscience.gov.au/dataset/ga/115066>
- 726 Beaman, R.J., 2018b. High-resolution depth model for Northern Australia - 30 m [WWW
727 Document]. Geoscience Australia. URL
728 <http://pid.geoscience.gov.au/dataset/ga/121620>
- 729 Bearup, D., Blasius, B., 2017. Ecotone formation induced by the effects of tidal flooding: A
730 conceptual model of the mud flat-coastal wetland ecosystem. *Ecological Complexity*
731 32, 217–227.
- 732 Bell, P.S., Bird, C.O., Plater, A.J., 2016. A temporal waterline approach to mapping intertidal
733 areas using X-band marine radar. *Coastal Engineering* 107, 84–101.
734 <https://doi.org/10.1016/j.coastaleng.2015.09.009>
- 735 Billerbeck, M., Werner, U., Bosselmann, K., Walpersdorf, E., Huettel, M., 2006. Nutrient
736 release from an exposed intertidal sand flat. *Marine Ecology Progress Series* 316,
737 35–51.
- 738 Bishop-Taylor, R., Sagar, S., Lymburner, L., 2018. National Intertidal Digital Elevation Model
739 25m 1.0.0 [WWW Document]. Geoscience Australia. URL
740 <http://dx.doi.org/10.26186/5c4fc06a79f76>
- 741 Boak, E.H., Turner, I.L., 2005. Shoreline definition and detection: A review. *Journal of*
742 *Coastal Research* 688–703. <https://doi.org/10.2112/03-0071.1>
- 743 Bugnot, A.B., Lyons, M.B., Scanes, P., Clark, G.F., Fyfe, S.K., Lewis, A., Johnston, E.L.,
744 2018. A novel framework for the use of remote sensing for monitoring catchments at

- 745 continental scales. *Journal of Environmental Management* 217, 939–950.
746 <https://doi.org/10.1016/j.jenvman.2018.03.058>
- 747 Bunt, J.S., Williams, W.T., Bunt, E.D., 1985. Mangrove species distribution in relation to tide
748 at the seafront and up rivers. *Marine and Freshwater Research* 36, 481–492.
- 749 Chen, L.C., Rau, J.Y., 1998. Detection of shoreline changes for tideland areas using multi-
750 temporal satellite images. *International Journal of Remote Sensing* 19, 3383–3397.
- 751 Chen, W.-W., Chang, H.-K., 2009. Estimation of shoreline position and change from satellite
752 images considering tidal variation. *Estuarine, Coastal and Shelf Science* 84, 54–60.
753 <https://doi.org/10.1016/j.ecss.2009.06.002>
- 754 Chen, Y., Dong, J., Xiao, X., Zhang, M., Tian, B., Zhou, Y., Li, B., Ma, Z., 2016. Land claim
755 and loss of tidal flats in the Yangtze Estuary. *Scientific Reports* 6, 24018.
756 <https://doi.org/10.1038/srep24018>
- 757 Chmura, G.L., Anisfeld, S.C., Cahoon, D.R., Lynch, J.C., 2003. Global carbon sequestration
758 in tidal, saline wetland soils. *Global Biogeochemical Cycles* 17.
- 759 Danaher, T., Collett, L., 2006. Development, optimisation and multi-temporal application of a
760 simple Landsat based water index, in: *Proceeding of the 13th Australasian Remote*
761 *Sensing and Photogrammetry Conference*, Canberra, ACT, Australia.
- 762 Dhanjal-Adams, K.L., Hanson, J.O., Murray, N.J., Phinn, S.R., Wingate, V.R., Mustin, K.,
763 Lee, J.R., Allan, J.R., Cappadonna, J.L., Studds, C.E., Clemens, R.S., Roelfsema,
764 C.M., Fuller, R.A., 2016. The distribution and protection of intertidal habitats in
765 Australia. *Emu* 116, 208. <https://doi.org/10.1071/MU15046>
- 766 Dhu, T., Dunn, B., Lewis, B., Lymburner, L., Mueller, N., Telfer, E., Lewis, A., McIntyre, A.,
767 Minchin, S., Phillips, C., 2017. Digital earth Australia – unlocking new value from
768 earth observation data. *Big Earth Data* 1, 64–74.
769 <https://doi.org/10.1080/20964471.2017.1402490>
- 770 Donaldson, P., Sharples, C., Anders, R.J., 2012. The tidal characteristics and shallow-
771 marine seagrass sedimentology of Robbins Passage and Boullanger Bay, far
772 northwest Tasmania (A technical report to Cradle Coast Natural Resource
773 Management). Blue Wren Group, School of Geography and Environmental Studies,
774 University of Tasmania, Hobart.
- 775 Drusch, M., Del Bello, U., Carlier, S., Colin, O., Fernandez, V., Gascon, F., Hoersch, B.,
776 Isola, C., Laberinti, P., Martimort, P., 2012. Sentinel-2: ESA's optical high-resolution
777 mission for GMES operational services. *Remote Sensing of Environment* 120, 25–36.
- 778 Dwyer, J.L., Roy, D.P., Sauer, B., Jenkerson, C.B., Zhang, H.K., Lymburner, L., 2018.
779 Analysis ready data: Enabling analysis of the Landsat archive. *Remote Sensing* 10,
780 1363. <https://doi.org/10.3390/rs10091363>

- 781 Eakins, B.W., Grothe, P.R., 2014. Challenges in building coastal digital elevation models.
782 Journal of Coastal Research 942–953. <https://doi.org/10.2112/JCOASTRES-D-13->
783 00192.1
- 784 Egbert, G.D., Erofeeva, S.Y., 2010. The OSU TOPEX/Poseidon Global Inverse Solution
785 TPXO [WWW Document]. TPXO8-atlas Version 1.0. URL
786 <http://volkov.oce.orst.edu/tides/global.html> (accessed 2.15.16).
- 787 Egbert, G.D., Erofeeva, S.Y., 2002. Efficient inverse modeling of barotropic ocean tides. *J.*
788 *Atmos. Oceanic Technol.* 19, 183–204. <https://doi.org/10.1175/1520->
789 0426(2002)019<0183:EIMOBO>2.0.CO;2
- 790 Egorov, A., Roy, D., Zhang, H., Hansen, M., Kommareddy, A., Egorov, A.V., Roy, D.P.,
791 Zhang, H.K., Hansen, M.C., Kommareddy, A., 2018. Demonstration of percent tree
792 cover mapping using landsat analysis ready data (ARD) and sensitivity with respect
793 to landsat ard processing level. *Remote Sensing* 10, 209.
794 <https://doi.org/10.3390/rs10020209>
- 795 Eleveld, M.A., van der Wal, D., van Kessel, T., 2014. Estuarine suspended particulate matter
796 concentrations from sun-synchronous satellite remote sensing: Tidal and
797 meteorological effects and biases. *Remote sensing of environment* 143, 204–215.
- 798 Fan, Y., Chen, S., Zhao, B., Yu, S., Ji, H., Jiang, C., 2018. Monitoring tidal flat dynamics
799 affected by human activities along an eroded coast in the Yellow River Delta, China.
800 *Environmental Monitoring and Assessment* 190, 396.
- 801 Flood, N., 2013. Seasonal composite Landsat TM/ETM+ images using the medoid (a multi-
802 dimensional median). *Remote Sensing* 5, 6481–6500.
- 803 Galbraith, H., Jones, R., Park, R., Clough, J., Herrod-Julius, S., Harrington, B., Page, G.,
804 2002. Global climate change and sea level rise: potential losses of intertidal habitat
805 for shorebirds. *Waterbirds* 25, 173–183.
- 806 Gallant, J., Dowling, T., Read, A., Wilson, N., Tickle, P., Inskeep, C., 2010. 1 second SRTM
807 derived digital elevation model user guide. Geoscience Australia, Canberra, ACT.
- 808 Gao, J., 2009. Bathymetric mapping by means of remote sensing: methods, accuracy and
809 limitations. *Progress in Physical Geography* 33, 103–116.
810 <https://doi.org/10.1177/0309133309105657>
- 811 García-Rubio, G., Huntley, D., Russell, P., 2015. Evaluating shoreline identification using
812 optical satellite images. *Marine Geology* 359, 96–105.
813 <https://doi.org/10.1016/j.margeo.2014.11.002>
- 814 GDAL/OGR contributors, 2018. GDAL/OGR Geospatial Data Abstraction software library
815 [WWW Document]. Open Source Geospatial Foundation. URL <http://gdal.org>

- 816 Gens, R., 2010. Remote sensing of coastlines: detection, extraction and monitoring.
817 International Journal of Remote Sensing 31, 1819–1836.
818 <https://doi.org/10.1080/01431160902926673>
- 819 Geoscience Australia, 2015. Digital Elevation Model (DEM) of Australia derived from LiDAR
820 5 Metre Grid [WWW Document]. URL <http://pid.geoscience.gov.au/dataset/ga/89644>
821 (accessed 9.25.18).
- 822 Gharibreza, M., Habibi, A., Imamjomeh, S.R., Ashraf, M.A., 2014. Coastal processes and
823 sedimentary facies in the Zohreh River Delta (Northern Persian Gulf). *Catena* 122,
824 150–158.
- 825 Gorelick, N., Hancher, M., Dixon, M., Ilyushchenko, S., Thau, D., Moore, R., 2017. Google
826 Earth Engine: Planetary-scale geospatial analysis for everyone. *Remote Sensing of*
827 *Environment, Big Remotely Sensed Data: tools, applications and experiences* 202,
828 18–27. <https://doi.org/10.1016/j.rse.2017.06.031>
- 829 Hagenaaars, G., de Vries, S., Luijendijk, A.P., de Boer, W.P., Reniers, A.J., 2018. On the
830 accuracy of automated shoreline detection derived from satellite imagery: A case
831 study of the Sand Motor mega-scale nourishment. *Coastal Engineering* 133, 113–
832 125.
- 833 Hermosilla, T., Wulder, M.A., White, J.C., Coops, N.C., Hobart, G.W., 2017. Updating
834 Landsat time series of surface-reflectance composites and forest change products
835 with new observations. *International Journal of Applied Earth Observation and*
836 *Geoinformation* 63, 104–111. <https://doi.org/10.1016/j.jag.2017.07.013>
- 837 Hogrefe, K.R., Wright, D.J., Hochberg, E.J., 2008. Derivation and integration of shallow-
838 water bathymetry: implications for coastal terrain modeling and subsequent analyses.
839 *Marine Geodesy* 31, 299–317. <https://doi.org/10.1080/01490410802466710>
- 840 Hsu, T.-J., Chen, S.-N., Ogston, A.S., 2013. The landward and seaward mechanisms of fine-
841 sediment transport across intertidal flats in the shallow-water region—A numerical
842 investigation. *Continental Shelf Research* 60, S85–S98.
- 843 HydroSurvey Australia, 2009. Report for bathymetric and benthic survey of the proposed
844 East Point outfall (No. Part 2), Bathymetric Report No. Survey No. 018_08. Power
845 and Water Corporation/GHD.
- 846 Isenburg, M., 2018. LAStools-efficient tools for LiDAR processing [WWW Document]. URL
847 <http://www.cs.unc.edu/~isenburg/lastools/>
- 848 Jones, E., Oliphant, T., Peterson, P., 2014. {SciPy}: open source scientific tools for {Python}.
- 849 Kelly, J.T., Gontz, A.M., 2018. Using GPS-surveyed intertidal zones to determine the validity
850 of shorelines automatically mapped by Landsat water indices. *International Journal of*
851 *Applied Earth Observation and Geoinformation* 65, 92–104.

- 852 Kirwan, M.L., Megonigal, J.P., 2013. Tidal wetland stability in the face of human impacts and
853 sea-level rise. *Nature* 504, 53–60. <https://doi.org/10.1038/nature12856>
- 854 Klemas, V., 2011. Beach profiling and LIDAR bathymetry: An overview with case studies.
855 *Journal of Coastal Research* 1019–1028. [https://doi.org/10.2112/JCOASTRES-D-11-](https://doi.org/10.2112/JCOASTRES-D-11-00017.1)
856 00017.1
- 857 Lewis, A., Lymburner, L., Purss, M.B.J., Brooke, B., Evans, B., Ip, A., Dekker, A.G., Irons,
858 J.R., Minchin, S., Mueller, N., Oliver, S., Roberts, D., Ryan, B., Thankappan, M.,
859 Woodcock, R., Wyborn, L., 2016. Rapid, high-resolution detection of environmental
860 change over continental scales from satellite data – the Earth Observation Data
861 Cube. *International Journal of Digital Earth* 9, 106–111.
862 <https://doi.org/10.1080/17538947.2015.1111952>
- 863 Li, W., Gong, P., 2016. Continuous monitoring of coastline dynamics in western Florida with
864 a 30-year time series of Landsat imagery. *Remote Sensing of Environment* 179,
865 196–209. <https://doi.org/10.1016/j.rse.2016.03.031>
- 866 Liu, Y., Li, M., Mao, L., Cheng, L., Li, F., 2013a. Toward a method of constructing tidal flat
867 digital elevation models with MODIS and medium-resolution satellite images. *Journal*
868 *of Coastal Research* 438–448. <https://doi.org/10.2112/JCOASTRES-D-12-00088.1>
- 869 Liu, Y., Li, M., Zhou, M., Yang, K., Mao, L., 2013b. Quantitative analysis of the waterline
870 method for topographical mapping of tidal flats: A case study in the Dongsha
871 Sandbank, China. *Remote Sensing* 5, 6138–6158. <https://doi.org/10.3390/rs5116138>
- 872 Lorensen, W.E., Cline, H.E., 1987. Marching cubes: A high resolution 3D surface
873 construction algorithm, in: *ACM Siggraph Computer Graphics*. ACM, pp. 163–169.
- 874 Lowe, R.J., Leon, A.S., Symonds, G., Falter, J.L., Gruber, R., 2015. The intertidal hydraulics
875 of tide-dominated reef platforms. *J. Geophys. Res. Oceans* 120, 4845–4868.
876 <https://doi.org/10.1002/2015JC010701>
- 877 Luijendijk, A., Hagenaars, G., Ranasinghe, R., Baart, F., Donchyts, G., Aarninkhof, S., 2018.
878 The state of the world's beaches. *Scientific Reports* 8, 6641.
879 <https://doi.org/10.1038/s41598-018-24630-6>
- 880 Mason, D., Davenport, I., Flather, R., Gurney, C., Robinson, G., Smith, J., 2001. A sensitivity
881 analysis of the waterline method of constructing a digital elevation model for intertidal
882 areas in ERS SAR scene of Eastern England. *Estuarine, Coastal and Shelf Science*
883 53, 759–778.
- 884 Mason, D.C., Davenport, I.J., Robinson, G.J., Flather, R.A., McCartney, B.S., 1995.
885 Construction of an inter-tidal digital elevation model by the 'Water-Line' Method.
886 *Geophys. Res. Lett.* 22, 3187–3190. <https://doi.org/10.1029/95GL03168>

- 887 Mason, D.C., Hill, D., Davenport, I., Flather, R., Robinson, G., 1997. Improving inter-tidal
888 digital elevation models constructed by the waterline technique. Presented at the
889 Third ERS Symposium on Space at the service of our Environment, p. 1079.
- 890 Mason, D.C., Scott, T.R., Dance, S.L., 2010. Remote sensing of intertidal morphological
891 change in Morecambe Bay, U.K., between 1991 and 2007. *Estuarine, Coastal and*
892 *Shelf Science* 87, 487–496. <https://doi.org/10.1016/j.ecss.2010.01.015>
- 893 McFeeters, S.K., 1996. The use of the Normalized Difference Water Index (NDWI) in the
894 delineation of open water features. *International Journal of Remote Sensing* 17,
895 1425–1432. <https://doi.org/10.1080/01431169608948714>
- 896 McKinney, W., 2011. pandas: a foundational Python library for data analysis and statistics.
897 *Python for High Performance and Scientific Computing* 1–9.
- 898 Montgomery, J., Bryan, K., Horstman, E., Mullarney, J., 2018. Attenuation of Tides and
899 Surges by Mangroves: Contrasting Case Studies from New Zealand. *Water* 10, 1119.
- 900 Mueller, N., Lewis, A., Roberts, D., Ring, S., Melrose, R., Sixsmith, J., Lymburner, L.,
901 McIntyre, A., Tan, P., Curnow, S., Ip, A., 2016. Water observations from space:
902 Mapping surface water from 25 years of Landsat imagery across Australia. *Remote*
903 *Sensing of Environment* 174, 341–352. <https://doi.org/10.1016/j.rse.2015.11.003>
- 904 Murray, N.J., Ma, Z., Fuller, R.A., 2015. Tidal flats of the Yellow Sea: A review of ecosystem
905 status and anthropogenic threats. *Austral Ecology* 40, 472–481.
906 <https://doi.org/10.1111/aec.12211>
- 907 Murray, N.J., Phinn, S.R., Clemens, R.S., Roelfsema, C.M., Fuller, R.A., 2012. Continental
908 scale mapping of tidal flats across East Asia using the Landsat archive. *Remote*
909 *Sensing* 4, 3417–3426. <https://doi.org/10.3390/rs4113417>
- 910 Murray, N.J., Phinn, S.R., DeWitt, M., Ferrari, R., Johnston, R., Lyons, M.B., Clinton, N.,
911 Thau, D., Fuller, R.A., 2018. The global distribution and trajectory of tidal flats. *Nature*
912 1.
- 913 Pardo-Pascual, J.E., Sánchez-García, E., Almonacid-Caballer, J., Palomar-Vázquez, J.M.,
914 Priego de los Santos, E., Fernández-Sarría, A., Balaguer-Beser, Á., 2018. Assessing
915 the accuracy of automatically extracted shorelines on microtidal beaches from
916 Landsat 7, Landsat 8 and Sentinel-2 imagery. *Remote Sensing* 10, 326.
- 917 Parke, M.E., Stewart, R.H., Farless, D.L., Cartwright, D.E., 1987. On the choice of orbits for
918 an altimetric satellite to study ocean circulation and tides. *Journal of Geophysical*
919 *Research: Oceans* 92, 11693–11707.
- 920 Purcell, S., 2002. Intertidal reefs under extreme tidal flux in Buccaneer Archipelago, Western
921 Australia. *Coral Reefs* 21, 191–192.

- 922 Roberts, D., Mueller, N., McIntyre, A., 2017. High-dimensional pixel composites from Earth
923 Observation time series. *IEEE Transactions on Geoscience and Remote Sensing*
924 PP, 1–11. <https://doi.org/10.1109/TGRS.2017.2723896>
- 925 Rodríguez, J.F., Saco, P.M., Sandi, S., Saintilan, N., Riccardi, G., 2017. Potential increase in
926 coastal wetland vulnerability to sea-level rise suggested by considering
927 hydrodynamic attenuation effects. *Nature communications* 8, 16094.
- 928 Rogers, K., Lymburner, L., Salum, R., Brooke, B.P., Woodroffe, C.D., 2017. Mapping of
929 mangrove extent and zonation using high and low tide composites of Landsat data.
930 *Hydrobiologia* 803, 49–68. <https://doi.org/10.1007/s10750-017-3257-5>
- 931 Ryu, J.-H., Cho, W.-J., Won, J.-S., 2001. Estimation of the sedimentation budget in tidal flat
932 using remotely sensed data. Presented at the Geoscience and Remote Sensing
933 Symposium, 2001. IGARSS'01. IEEE 2001 International, IEEE, pp. 2409–2411.
- 934 Ryu, J.-H., Kim, C.-H., Lee, Y.-K., Won, J.-S., Chun, S.-S., Lee, S., 2008. Detecting the
935 intertidal morphologic change using satellite data. *Estuarine, Coastal and Shelf*
936 *Science* 78, 623–632. <https://doi.org/10.1016/j.ecss.2008.01.020>
- 937 Ryu, J.-H., Won, J.-S., Min, K.D., 2002. Waterline extraction from Landsat TM data in a tidal
938 flat: A case study in Gomso Bay, Korea. *Remote Sensing of Environment* 83, 442–
939 456. [https://doi.org/10.1016/S0034-4257\(02\)00059-7](https://doi.org/10.1016/S0034-4257(02)00059-7)
- 940 Sagar, S., Phillips, C., Bala, B., Roberts, D., Lymburner, L., 2018. Generating continental
941 scale pixel-based surface reflectance composites in coastal regions with the use of a
942 multi-resolution tidal model. *Remote Sensing* 10, 480.
943 <https://doi.org/10.3390/rs10030480>
- 944 Sagar, S., Roberts, D., Bala, B., Lymburner, L., 2017. Extracting the intertidal extent and
945 topography of the Australian coastline from a 28 year time series of Landsat
946 observations. *Remote Sensing of Environment* 195, 153–169.
947 <https://doi.org/10.1016/j.rse.2017.04.009>
- 948 Scrosati, R.A., Knox, A.S., Valdivia, N., Molis, M., 2011. Species richness and diversity
949 across rocky intertidal elevation gradients in Helgoland: testing predictions from an
950 environmental stress model. *Helgoland marine research* 65, 91.
- 951 Serra, J., 1983. *Image analysis and mathematical morphology*. Academic Press, Inc.
- 952 Sharples, C., Mount, R., Pedersen, T., 2009. The Australian coastal Smartline geomorphic
953 and stability map version 1: manual and data dictionary. Report of the University of
954 Tasmania for the Department of Climate Change and Geoscience Australia.
- 955 Skinner, C.J., Coulthard, T.J., Parsons, D.R., Ramirez, J.A., Mullen, L., Manson, S., 2015.
956 Simulating tidal and storm surge hydraulics with a simple 2D inertia based model, in
957 the Humber Estuary, UK. *Estuarine, Coastal and Shelf Science* 155, 126–136.

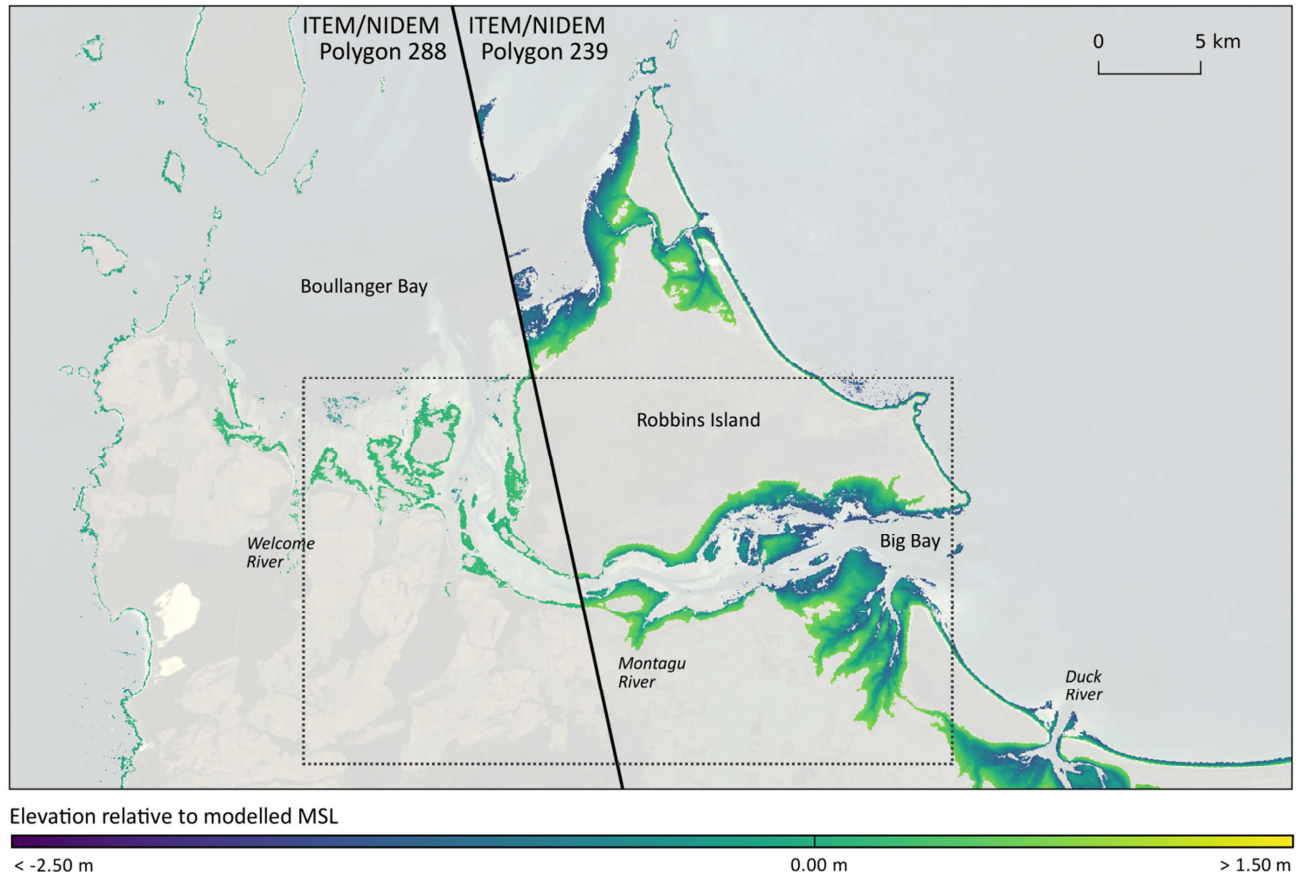
- 958 Smolders, S., Plancke, Y., Ides, S., Meire, P., Temmerman, S., 2015. Role of intertidal
959 wetlands for tidal and storm tide attenuation along a confined estuary: a model study.
960 *Natural Hazards and Earth Systems Sciences* 15, 1659–1675.
- 961 Solihuddin, T., O'Leary, M.J., Blakeway, D., Parnum, I., Kordi, M., Collins, L.B., 2016.
962 Holocene reef evolution in a macrotidal setting: Buccaneer Archipelago, Kimberley
963 Bioregion, Northwest Australia. *Coral Reefs* 1–12. [https://doi.org/10.1007/s00338-](https://doi.org/10.1007/s00338-016-1424-1)
964 016-1424-1
- 965 Spruzen, F.L., Richardson, A.M., Woehler, E.J., 2008. Spatial variation of intertidal
966 macroinvertebrates and environmental variables in Robbins Passage wetlands, NW
967 Tasmania. *Hydrobiologia* 598, 325–342.
- 968 Su, H., Liu, H., Heyman, W.D., 2008. Automated derivation of bathymetric information from
969 multi-spectral satellite imagery using a non-linear inversion model. *Marine Geodesy*
970 31, 281–298. <https://doi.org/10.1080/01490410802466652>
- 971 Temmerman, S., Meire, P., Bouma, T.J., Herman, P.M., Ysebaert, T., De Vriend, H.J., 2013.
972 Ecosystem-based coastal defence in the face of global change. *Nature* 504, 79.
- 973 Thieler, E.R., Danforth, W.W., 1994. Historical shoreline mapping (I): improving techniques
974 and reducing positioning errors. *Journal of Coastal Research* 549–563.
- 975 Thorner, J., Kumar, L., Smith, S.D., 2014. Impacts of climate-change-driven sea level rise on
976 intertidal rocky reef habitats will be variable and site specific. *PloS one* 9, e86130.
- 977 Tseng, K.-H., Kuo, C.-Y., Lin, T.-H., Huang, Z.-C., Lin, Y.-C., Liao, W.-H., Chen, C.-F., 2017.
978 Reconstruction of time-varying tidal flat topography using optical remote sensing
979 imageries. *ISPRS Journal of Photogrammetry and Remote Sensing* 131, 92–103.
980 <https://doi.org/10.1016/j.isprsjprs.2017.07.008>
- 981 Valdivia, N., Scrosati, R.A., Molis, M., Knox, A.S., 2011. Variation in community structure
982 across vertical intertidal stress gradients: how does it compare with horizontal
983 variation at different scales? *PLoS One* 6, e24062.
- 984 Van der Walt, S., Schönberger, J.L., Nunez-Iglesias, J., Boulogne, F., Warner, J.D., Yager,
985 N., Guillaud, E., Yu, T., 2014. scikit-image: image processing in Python. *PeerJ* 2,
986 e453.
- 987 Wang, X., Xiao, X., Zou, Z., Chen, B., Ma, J., Dong, J., Doughty, R.B., Zhong, Q., Qin, Y.,
988 Dai, S., 2018. Tracking annual changes of coastal tidal flats in China during 1986–
989 2016 through analyses of Landsat images with Google Earth Engine. *Remote*
990 *Sensing of Environment*.
- 991 Weatherall, P., Marks, K.M., Jakobsson, M., Schmitt, T., Tani, S., Arndt, J.E., Rovere, M.,
992 Chayes, D., Ferrini, V., Wigley, R., 2015. A new digital bathymetric model of the
993 world's oceans. *Earth and Space Science* 2, 331–345.
994 <https://doi.org/10.1002/2015EA000107>

- 995 White, J.C., Wulder, M.A., Hobart, G.W., Luther, J.E., Hermosilla, T., Griffiths, P., Coops,
996 N.C., Hall, R.J., Hostert, P., Dyk, A., Guindon, L., 2014. Pixel-Based Image
997 compositing for large-area dense time series applications and science. *Canadian*
998 *Journal of Remote Sensing* 40, 192–212.
999 <https://doi.org/10.1080/07038992.2014.945827>
- 1000 Whiteway, T., 2009. Australian bathymetry and topography grid. Geoscience Australia,
1001 Canberra.
- 1002 Williams, R.J., Watford, F.A., 1997. Identification of structures restricting tidal flow in New
1003 South Wales, Australia. *Wetlands Ecology and Management* 5, 87–97.
- 1004 Woodcock, C.E., Allen, R., Anderson, M., Belward, A., Bindschadler, R., Cohen, W., Gao, F.,
1005 Goward, S.N., Helder, D., Helmer, E., Nemani, R., Oreopoulos, L., Schott, J.,
1006 Thenkabail, P.S., Vermote, E.F., Vogelmann, J., Wulder, M.A., Wynne, R., 2008.
1007 Free access to Landsat imagery. *Science* 320, 1011–1011.
1008 <https://doi.org/10.1126/science.320.5879.1011a>
- 1009 Wulder, M.A., Masek, J.G., Cohen, W.B., Loveland, T.R., Woodcock, C.E., 2012. Opening
1010 the archive: How free data has enabled the science and monitoring promise of
1011 Landsat. *Remote Sensing of Environment, Landsat Legacy Special Issue* 122, 2–10.
1012 <https://doi.org/10.1016/j.rse.2012.01.010>
- 1013 Xia, S., Yu, X., Millington, S., Liu, Y., Jia, Y., Wang, L., Hou, X., Jiang, L., 2017. Identifying
1014 priority sites and gaps for the conservation of migratory waterbirds in China's coastal
1015 wetlands. *Biological Conservation, Special Issue on China's Biodiversity*
1016 *Conservation* 210, 72–82. <https://doi.org/10.1016/j.biocon.2016.07.025>
- 1017 Xu, H., 2006. Modification of normalised difference water index (NDWI) to enhance open
1018 water features in remotely sensed imagery. *International Journal of Remote Sensing*
1019 27, 3025–3033. <https://doi.org/10.1080/01431160600589179>
- 1020 Xu, N., 2018. Detecting Coastline Change with All Available Landsat Data over 1986–2015:
1021 A Case Study for the State of Texas, USA. *Atmosphere* 9, 107.
- 1022 Xu, Z., Kim, D., Kim, S.H., Cho, Y.-K., Lee, S.-G., 2016. Estimation of seasonal topographic
1023 variation in tidal flats using waterline method: A case study in Gomso and
1024 Hampyeong Bay, South Korea. *Estuarine, Coastal and Shelf Science* 183, 213–220.
1025 <https://doi.org/10.1016/j.ecss.2016.10.026>
- 1026 Zhao, B., Guo, H., Yan, Y., Wang, Q., Li, B., 2008. A simple waterline approach for tidelands
1027 using multi-temporal satellite images: A case study in the Yangtze Delta. *Estuarine*
1028 *Coastal and Shelf Science* 77, 134–142. <https://doi.org/10.1016/j.ecss.2007.09.022>
- 1029

1030 Appendix A

1031 Figure A1. Location of the Robbins Island validation site (dotted grey line), displaying the
1032 discontinuities in NIDEM elevations in Boullanger Bay at either side of the boundary of two
1033 tidal modelling polygons (dark black line).

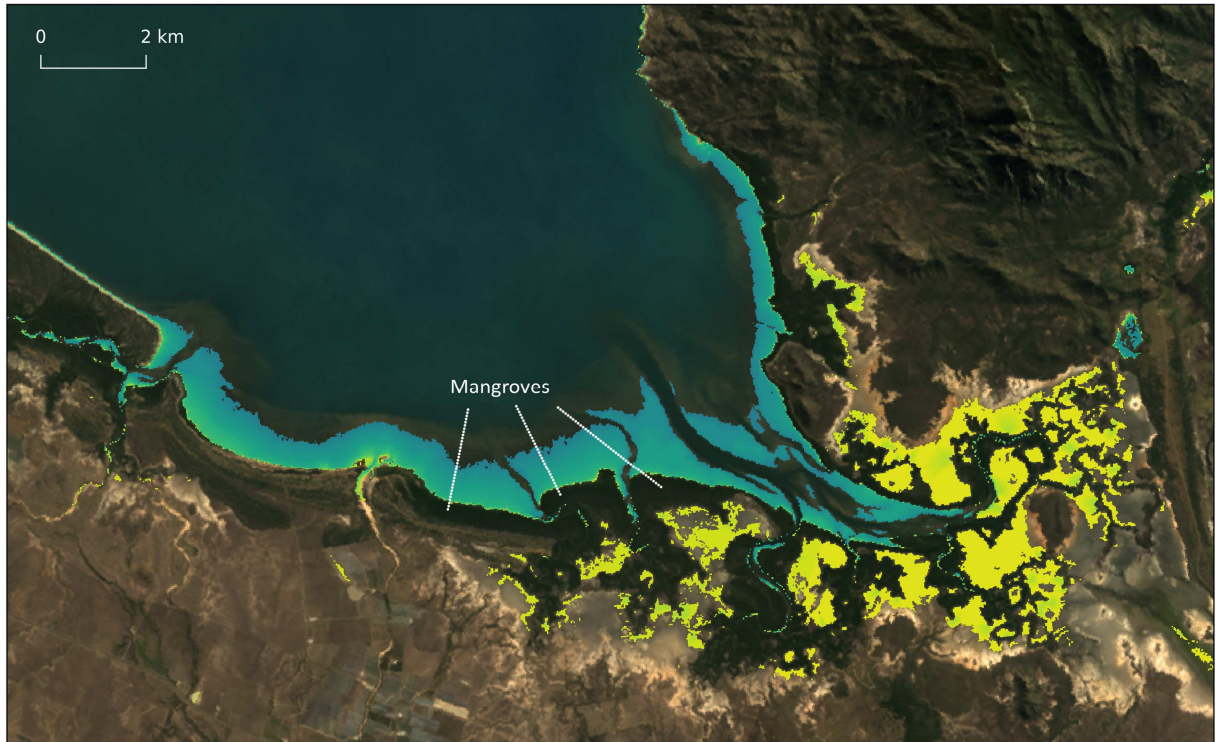
1034



1035

1036

1037 Figure A2. NIDEM data for the Whitsunday validation site, highlighting the lack of modelled
1038 intertidal terrain in mangrove areas (dark green vegetation) and the presence of modelled
1039 elevations in areas on the landward side of mangrove communities inundated only during
1040 the highest tides.
1041



Elevation relative to modelled MSL

< -2.50 m

0.00 m

> 1.50 m

1042

ACCEPTED